MECHANICAL & TRIBOCORROSION BEHAVIOUR OF ULTRA-FINE GRAINED 316L STAINLESS STEEL

A **DISSERTATION**

Submitted in partial fulfilment of the

requirements for the award of the degree of

MASTER OF TECHNOLOGY

in

METALLURGICAL AND MATERIALS ENGINEERING

(With specialization in Industrial Metallurgy)

By

MITTA DIVYA

DEPARTMENT OF METALLURGICAL AND MATERIALS ENGINEERING

INDIAN INSTITUTE OF TECHNOLOGY ROORKEE

ROORKEE- 247 667 (INDIA)

MAY, 2016

CANDIDATE'S DECLARATION

I hereby declare that the proposed work presented in this dissertation entitled "Mechanical and tribocorrosion behaviour of ultra fine grained 316L stainless steel" is in partial fulfilment of the requirements for the award of the degree of **MASTER OF TECHNOLOGY** in **METALLURGICAL AND MATERIALS ENGINEERING** with specialization in **INDUSTRIAL METALLURGY**, submitted in the **Department of Metallurgical and Materials Engineering**, **Indian Institute of Technology Roorkee** is an authentic record of my own work carried out during the period from July 2015 to May 2016 under the supervision of **Dr. G.P.Chaudhari**, Associate Professor, Department of Metallurgical and Materials Engineering, Indian Institute of Technology Roorkee, India.

The work presented in this dissertation has not been submitted by me for the award of any other degree.

Dated:

Place: Roorkee **MITTA DIVYA**

CERTIFICATE

This is to certify that the above statement made by the candidate is correct to the best of my knowledge and belief.

Dr. G.P. CHAUDHARI

Associate Professor

Department of Metallurgical &Materials

Engineering

Indian Institute of Technology, Roorkee

Roorkee- 247667 (INDIA)

ACKNOWLEDGEMENTS

I take this opportunity to my deep gratitude and sincere thanks to Dr G.P.Chaudhari, Associate Professor, Department of Metallurgical and Materials Engineering, IIT Roorkee for his expert and kind guidance to my thesis work. My work would have been directionless without his constant and patient guidance. I believe that the things that I have learnt from him will benefit me over the course of my lifetime.

I would like to thank our respected Head of the Department Dr.Anjan Sil and all faculty members of the department for providing all the facilities required to carry out the work. I would also like to thank the technical staff at the department in helping me access the lab and equipment. I would also like to express my sincere thanks to Mr.BrijKishor, Mr. R. Sunil Kumar for their scientific help, inspiration, and valuable suggestions throughout the tenure. My sincere thanks to my friends Mr. Vignesh Sreenivas, Ms. Nikita Goel, and Mr. Neeraj Kumar Prasad, for encouraging and helping me in all aspects of my work.

Finally, I would like to express my heartiest gratitude to my parents, Mr. M CH Chennaiah and Mrs. M Anjili Devi for showering their blessings over me. I would also like to thank my brother Mr. M Ravi Shankar and my beloved well wisher Mr. N Rahul Aasish, for their moral support and inspiration throughout my M.Tech course.

CONTENTS

LIST OF FIGURES

LIST OF TABLES

ABSTRACT

Stainless steels are primarily chosen for their corrosion resistance. Most commonly used grades are the non-magnetic austenitic kind. Using severe plastic deformation processes results in grain refinement which contributes for improved strength and weight saving for many applications. If the combined action of wear and corrosion, commonly known as the tribo-corrosion behaviour, of severely plastic deformation processed steel is comparable to the as-received steel then its use in biomedical implants, chemical processing equipment, and food-processing industries will be justified. Most of the orthopaedic implants fail due to combined action of wear and corrosion in the body fluids. Therefore, the main aim of the current work is to study the microstructural evolution and tribocorrosion behaviour of ultra-fine grained 316L stainless steel, a grade that can be used in body implants and other industrial applications. For microstructural analysis, optical microscopy, scanning electron microscopy and transmission electron microscopy was carried out, which showed extreme grain refinement in MAFed samples. Hardness testing was performed on multi-axially forged samples. Corrosion and tribocorrosion behaviour is evaluated which showed an improvement in uniform corrosion rate and wear resistance of MAFed samples in Hanks' solution.

CHAPTER 1: INTRODUCTION

Stainless steels are the most common engineering materials as they exhibit an excellent corrosion resistance. Stainless steels (SS) contain a minimum of 10.5% chromium that helps to form a passive film of chromium oxide. This chromium oxide film blocks the oxygen diffusion to the metal surface, thus protecting it from further corrosion.

Grade 316L is a standard molybdenum-bearing grade in austenitic SS, with approximately 2% molybdenum, which provides higher pitting and crevice corrosion resistance in chloride environments. It is a similar grade of 316 SS, but with lesser carbon content i.e., about 0.03% carbon, making 316L grade immune to sensitization. Thus, it is used in welded components. Its austenitic structure provides very good toughness even at cryogenic temperature. 316L SS also offers high creep resistance, stress to rupture and tensile strength at elevated temperatures [1]. Conventional applications include food preparation equipment particularly in chloride environments, jet engine components, parts used in marine environments, and tubing.

Developing ultra-fine grained (UFG) materials with superior properties is now increasingly common. In addition to strength, UFG materials possess excellent ductility, fatigue strength, toughness, wear resistance, and super-plasticity [2]. According to Hall-Petch relation, grain refinement results in a better yield strength [3]. Hence, when compared to common strengthening methods like phase hardening and strain hardening, grain refining methods offer an advantage of improving the yield strength without affecting ductility much [4]. Severe plastic deformation (SPD) processes induce high plastic strains in the materials to produce a UFG structure without changing the shape of the bulk specimen. Various common SPD processes include:

- Equal Channel Angular Pressing (ECAP)
- Accumulative Roll-Bonding (ARB)
- High Pressure Torsion (HPT)
- Multi-Axial Forging (MAF)

Warm MAF is a SPD process carried out near the recrystallisation temperature (< $0.5T_m$). In MAF process, the materials are forged by changing the compression axis by 90° after each pass thereby resulting in an equiaxed UFG structure. The main asset of MAF is the shape and dimensions of the material remains the same with less distortion even after several passes of forging [5]. UFG 316L with extreme high strength offers better corrosion resistance, higher inertness, and bio-compatibility needed for medical implants compared to the coarse grained counterpart with low strength and fatigue limit.

The combined effect of wear and corrosion leading to metal deterioration is termed as tribocorrosion. Tribocorrosion behaviour is observed in a large number of applications in different environments. Some typical examples of such occurrences include pistons, cylinders and valves in an engine, frames of an eyeglass (due to friction with the skin in the presence of perspiration), electrical connectors (during insertion and removal in a humid or corrosive environment), joint prostheses (when friction occurs in a physiological liquid), and components used in plumbing and pump technology. Medical implants such as pins, screws and orthopaedic implants like total hip and knee replacements undergo scratching, abrasion and erosion in a corrosive body fluid [6]. Here, the UFG material plays an important role due to its excellent strength, toughness, fatigue strength and superior corrosion resistance in NaCl solution and simulated body fluid i.e., Hanks' solution.

Based on the above information, it is believed that UFG 316L can be employed for biomedical applications and applications in corrosive environments. The mechanical properties of such material will be better. However, the tribocorrosion behaviour is yet to be evaluated. A detailed literature survey is carried out before proceeding to the experimentation.

CHAPTER 2: LITERATURE REVIEW

2.1. PROCESSING OF UFG MATERIAL BY SPD

Deforming a material by applying ultra-large plastic strain is termed as severe plastic deformation, which leads to a UFG structure. According to Hall-Petch relation stated in equation (1), grain refinement by the process of SPD leads to an excellent increase in yield strength [3]. This can be explained by the piling up of dislocations at the grain boundaries during deformation, which restricts the grain boundary movement [7].

$$\sigma_y = \sigma_0 + kd^{-0.5} \quad (1)$$

Where,

σ_y = yield strength

σ_0 = material constant (stress required for dislocation movement)

k = strengthening coefficient

d = average grain diameter

Under SPD process, the material does not undergo any change in its shape thus making it amenable for structural applications. Among all the SPD processes available, MAF is best suited for steels used for biomedical and structural applications because of its nature to produce equiaxed grain structure while using the extant forging infrastructure.

MAF is chosen because the setup is relatively simple and can be commercialized easily. MAF is carried out on rectangular prismatic blocks. The forging axis changed from X to Y to Z after each forging pass by rotation of 90° as shown in Fig.1.

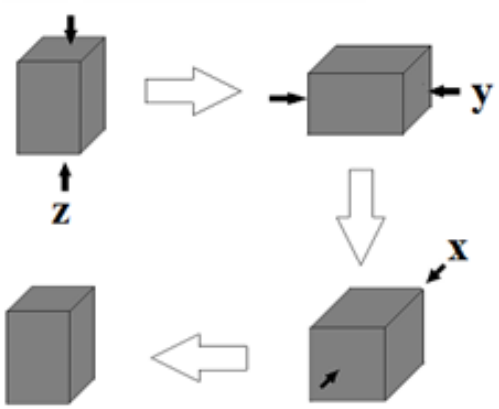

Fig.1. Representation of one cycle of MAF

There is a significant research going on other SPD processes to produce UFG structures. Zheng et al used the method of ECAP to evaluate the hybrid refining mechanism of 304 SS. However, increasing the number of ECAP extrusions (beyond 4–6) was not helpful in improving further grain refinement [8]. Pachla et al studied nano-structuring of 316L by hydrostatic extrusion wherein the formation of strain induced martensite increased with increasing strain [9].

Apart from SPD processes, some non-SPD methods like cryorolling followed by martensitic reversion induced by annealing for short periods, can also be used to get ultra fine grains [10]. However, this method leads to the formation of large amount of martensite, which being brittle decreases the ductility of the material and reduces the corrosion resistance of the material.

Eskandari et al studied the effect of strain-induced martensite on the formation of nano-crystalline 316L stainless steel after cold rolling and annealing [11]. The cold rolled steel contained a significant amount of martensite that increased exponentially in the deformation range. Wang et al produced nano-crystalline 316L by martensitic reversion [12]. Idell et al used plane-strain machining to produce UFG 316L with small volume fractions of strain-induced martensite that is detrimental for novel mechanical properties [13]. Therefore, using such methods leaves a large volume of martensite, which is detrimental for corrosion behaviour [14]. So these methods are not generally used these days to produce ultrafine grains.

2.2. MULTI-AXIAL FORGING OF 316L

Grain refinement by MAF technique is preferable because of its simplicity and easy availability. During the forging procedure, the axis of forging is changed after each pass by rotation of 90°. Depending on the processing parameters, the microstructure evolution of 316L is attributed to various mechanisms such as continuous dynamic recrystallisation (cDRX), dynamic recovery, martensitic transformation, and deformation twinning [15].

In warm MAF of austenitic Fe-Ni alloy at 600^{o}C, UFG structure is obtained as a result of cDRX [16]. In austenitic stainless steel multi-axially compressed at 600^{0}C, dynamic recovery assisted in an increase in mismatch between the sub grains with an increase in cumulative strain [17]. In MAF of super 304 H-type austenitic stainless steel to a cumulative strain of 4 at an ambient temperature, grain refinement is due to both the mechanical twinning and martensitic transformation [18].

316L being an austenitic SS, is a low stacking fault energy (SFE) material which builds up considerably higher dislocation densities during working when compared to metals that have high SFE**.** Eventually in low SFE materials, the accumulated dislocation density becomes sufficiently high to stimulate the nucleation of recrystallisation during hot deformation. This mechanism is referred to as dynamic recrystallisation (DRX).

2.2.1. CONTINUOUS DYNAMIC RECRYSTALLISATION

Ultra fine grained steel was obtained by means of deformation using multi-axial forging of austenitic steel at room temperature where DRX dominated [19]. However, it was also found out that refinement of the order of nano-size level or sub-micron size could be achieved during cDRX within a lower temperature range using SPD processes such as ARB, ECAP, MAF etc,.

The main aim of Huang et al [19] was to explain cDRX of multi-axially forged austenite and to subsequently explain the microstructural evolution. The development of CDRX mechanism during MAF is shown in Fig.2.

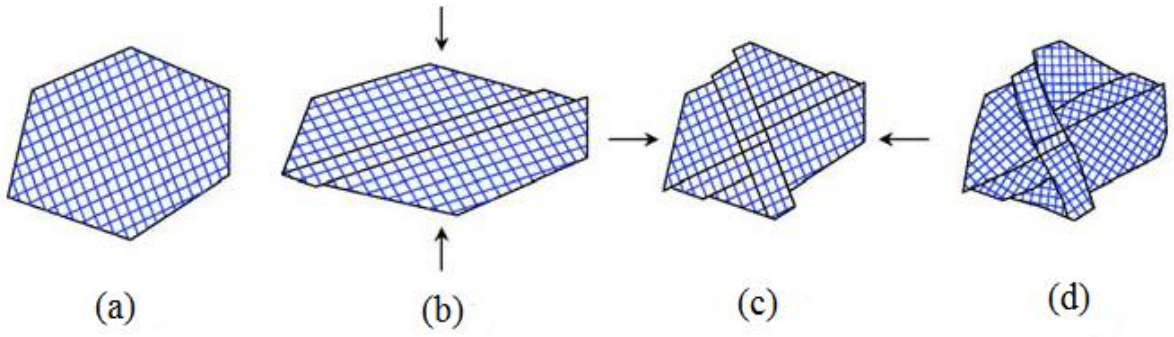

Fig.2. The evolution mechanism of cDRX during MAF (a) initial coarse grain structure comparatively, (b) after the first pass, (c) after the second pass with deformation direction rotated 90°, (d) sub-grain formation in the subsequent passes [19]

When deformation occurs in the initial grains in a certain direction, due to shear phenomenon in the deformed grains, deformation bands are generated along a certain direction. Deformed bands are also formed in other directions as the deformation direction changes. Thus, austenite grain is subdivided into various sub grains because of crossing of deformed bands. In addition, this sub grains so formed are slowly converted into new independent grains by forming high angle grain boundaries in further deformation passes.

Tikhonova et al [20] carried out MAF of 304 SS in warm conditions. The mechanism behind the grain refinement is cDRX. The process of nucleation and growth of new grains is a continuous phenomenon. At initial passes, the deformation produces misorientation of sub-grains with dislocations as sub boundaries. As the deformation progresses, the misorientation increases and eventually high angle grain boundaries (HAGB) are formed. An increase in the flow stress leads to smaller grain sizes. Lowering of the deformation temperature requires higher strains for cDRX to occur.

There have been several studies showing grain refinement due to MAF process. In 7475 Al alloy owing to MAF an average grain size of 9μm was obtained as compared to an initial grain size of 22μm [21]. In the case of MAF of magnesium alloy, average grain size of AZ80 alloy was reduced to 2 μm from an initial grain size of 136 μm [22].

In almost all the studies owing to MAF, strength and hardness of the material was increased as compared to the as-received material, but a huge drop in the ductility of material observed after repeated deformation cycles. In addition, there is less or no information about the behaviour of material in corrosive and wear environments.

2.3. TRIBOCORROSION

Tribocorrosion is a form of solid surface degradation due to the joint action of relatively moving mechanical contact and an electrochemical reaction, in which the damage may be more than either process acting separately. It leads to metal loss as wear, corrosion, and sometimes cracking occurs. These metal degradation processes induce significant problems in medical implants, offshore, mining, power generation and food processing applications. Therefore, it is very important to identify the contribution of combined action of corrosion and wear to material removal in the tribocorrosion process in order to evaluate the material performance.

The combined action of sliding and corrosion has recently become an issue of concern. Indeed, the electro-chemical growth and removal of passive films from the metal surface due to mechanical sliding, was the main reason for metal degradation [23].

Stainless steels, known for their passive behaviour, are one of the most commonly studied materials in recent tribocorrosion works. Many controlled tribocorrosion experiments were carried out on SS alloys immersed in H_2SO_4 [23] and NaCl solutions [24]. Sun et al [6] studied the tribocorrosion behaviour of AISI 304 SS in 0.5 M NaCl solution, where there is a dynamic competition between pit growth and wearing during the sliding process.

Suresh et al studied the tribocorrosion behaviour of equal channel angular extruded Ti-13Nb-13Zr alloy in simulated body fluid. There was a significant improvement in corrosion resistance of all UFG samples but for the as-received and the UFG samples, there was a noticeable difference in average friction coefficients [25]. Holmes et al studied the tribocorrosion of 316L in artificial saliva to make use of 316L in dental implants [26]. Salasi et al who worked on tribocorrosion of 316L showed that there was a significant change in the electrochemical response of passivating alloys during and post abrasion as the wear mechanism is altered [27].

From the above literature, it can be stated that some work is done on UFG materials. In addition, a number of materials are discovered to meet the needs of medical implants, structural, marine and architectural applications. However, with technological developments there is a need for even better strength, ductility, wear, and corrosion resistance. However, for structural and biomedical applications, UFG 316L produced by MAF can play an important role. Hence, the present work will be focussed to obtain UFG 316L with excellent properties that makes their usage more significant. The aim of the present study therefore is:

- To produce ultra-fine grained 316L SS by using MAF technique and to study its structure-mechanical property relationships
- To identify the effect of different factors like grain size, hardness, strength, ductility, on its tribocorrosion behaviour after different passes of MAF

CHAPTER 3: METHODOLOGY

- Processing: In the current research work, the as-received 316L austenitic SS was MAFed using 3 pass, 6 pass, 9 pass, and 12 pass in order to obtain a UFG material. For MAF, samples of size 20 mm x 16.3 mm x 13.3 mm were cut and subjected to strain of -0.4 per pass along the longest side of the sample. The dimensions were selected such that these were maintained after each forging pass during the MAF process, assuming conservation and isotropy of the material. Samples were heated to 630°C and after holding for 15 minutes they were alternately forged with the forging axis changed by 90° after each pass. After each forging pass, samples were quenched in water.
- Microstructure characterization: X-Ray Diffraction (XRD) analysis was done for all the MAFed and as-received samples to know the phases present and residual stresses, if any. Microstructure analysis of all the samples subjected to different passes of MAF was done using optical microscope as well as scanning electron microscope (SEM). Further to get a clear view about the refinement, the samples were observed in a transmission electron microscope (TEM).
- Mechanical characterization: Hardness measurements were carried out on a Vickers hardness tester with 10 kg load for all the samples and the trend from the as-received to 12 passed samples were observed and relation between Vickers hardness number and the number of passes was established.
- Corrosion behaviour: The corrosion behaviour of as-received and MAFed samples was evaluated in Hanks' solution, 3.5 wt% NaCl solution, and Ringers solution.
- Tribocorrosion characterization: The tribocorrosion behaviour of MAFed 316L in simulated body fluid i.e. Hanks' solution was studied.
- Analysis of results: All the results were analyzed with a view to meet the objectives.

CHAPTER 4: EXPERIMENTAL PROCEDURE

4.1. MATERIAL AND WARM MULTI-AXIAL FORGING PROCESS

A 316L type austenitic SS was investigated, where the chemical composition of the as-received material determined by Thermo Jarrell Ash spark emission spectroscopy is shown in Table 1.

Table 1 Chemical composition of 316L SS in weight percent

Element	**Cr**	**Ni**	**Mo**	**Mn**	**Si**	**Cu**	**C**	**Fe**
Wt%	16.63	10.06	2.26	0.64	0.57	0.20	0.03	69.61

For warm MAF, samples of size 20 mm x 16.3 mm x 13.3 mm were machined out. MAF was carried out on a 10^3 KN friction screw forging press shown in Fig.3. Uni-axial compressions of $\varepsilon = 0.4$ per strain step were applied along the longest side of the sample. Assuming conservation and isotropy of the material, open die forging was employed, where the dimensions of the samples were maintained after each forging pass with stopper blocks made of H-13 tool steel. The stopper blocks ensure that the applied strain is -0.4 per each pass and prevent any extra deformation.

Martensite formation affects the corrosion behaviour, hence it should be avoided during the severe warm working. So, the samples were heated to warm working temperatures ($<0.5T_m$) of around 630°C in an electric muffle furnace as shown in Fig.4. A holding time of 15 minutes is given to homogenise and maintain a uniform temperature throughout the sample. Long holding times leads to oxidation and decarburisation of the material which should be avoided.

Samples were now alternately forged by changing the forging axis by 90° after each pass (i.e., X – Y, Y – Z, Z – X). After each pass, the samples were quenched in water to suppress annihilation of dislocations to some extent and to prevent sensitization of austenitic SS.

Fig.3. Forging press with open die used for multi-axial forging

Graphite powder mixed in acetone was used as a lubricant to ensure relatively homogeneous deformation. The mixture was applied on to the forging die as a uniform layer. In the absence of proper lubrication, dead zones form where there is no plastic deformation which leads to non-uniform deformation.

Multi-axially forged samples were produced using 3, 6, 9 and 12 forging passes which will be studied further.

Fig.4. Muffle furnace for heating the samples prior to MAF

4.2. MICROSTRUCTURAL CHARACTERIZATION

After MAF, the as-received and MAFed samples were cut parallel along the last forging axis using Buehler Isomet 4000 saw shown in Fig.5. Samples were then successively polished using SiC emery paper starting from 320, 800, 1200, and 1500 grit size. To obtain a fine mirror-like surface, the samples were further polished on a velvet cloth with alumina of size 0.5 micron using a rotary cloth polisher. The samples were electro-etched using 60% HNO_3 at 2V for 20 seconds wherein the sample acts as an anode and a block of stainless steel was used as cathode.

Fig.5. Buehler Isomet 4000 saw used to cut the samples with required precision

Optical micrographs were obtained with Leica DMI 5000 M light optical microscope as shown in Fig.6. But due to the low magnifications available with the optical microscope, samples were observed under SEM for better understanding of grain refinement. SEM micrographs were obtained with LaB_6MA18 Zeiss SEM shown in Fig.7.

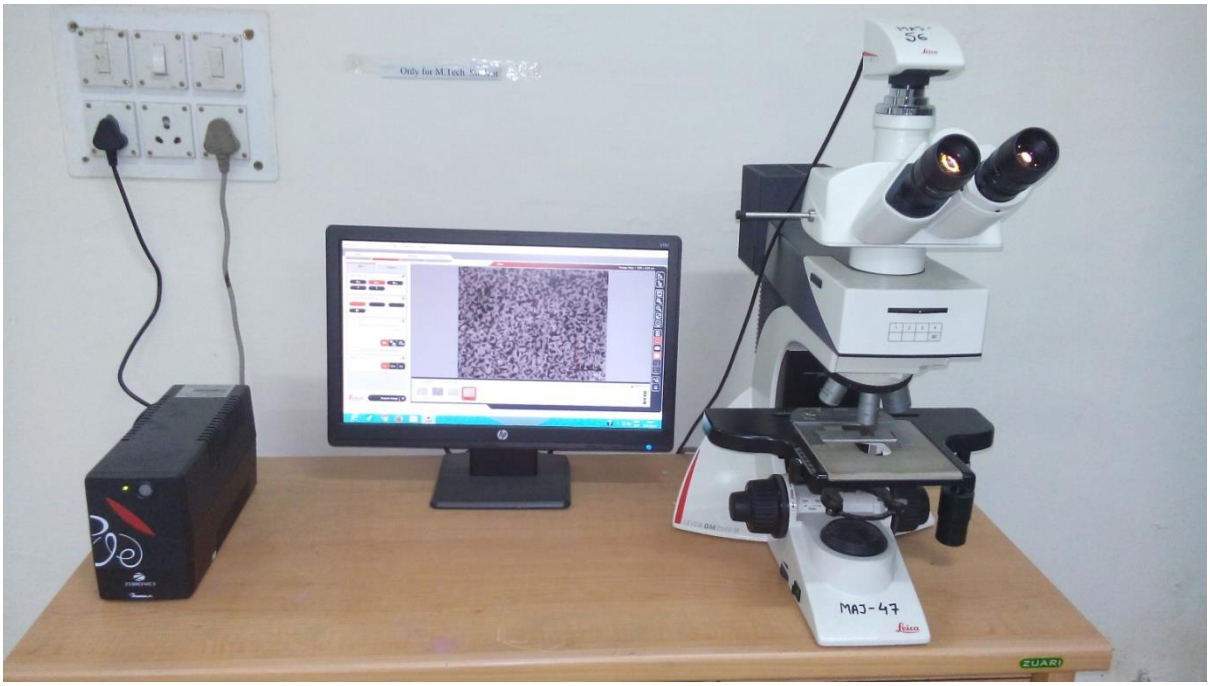

Fig.6.Leica DMI 5000 M light optical microscope

Fig.7. ZEISS scanning electron microscope used to observe the UFG microstructure

For XRD, a Bruker D8 Advance machine was used with Cu-Kα radiation in the angle range of 20° to 120° with a scan rate of 2°/min.

TEM imaging is carried on Tecnai G2 20, for which the samples were thinned to about 90 µm by mechanical polishing using SiC emery paper. Following which the samples were punched out as discs of 3 mm diameter. Twinjet electro-polishing is done at room temperature to create an electron transparent region. The etchant used for twinjet electro-polishing had a composition of 90% acetic acid and 10% perchloric acid.

4.3. HARDNESS TESTING

Hardness of the as-received and forged samples was measured using a FIE-VM50 PC Vickers hardness testing machine shown in Fig.8 by employing 10 kg load with a dwell time of 10 seconds. At-least six hardness readings were taken and the average is reported along with standard deviation.

Fig.8. FIE-VM50 PC Vickers hardness testing machine

4.4. CORROSION TESTING

As one of the end uses of the MAFed samples is in body implants, corrosion testing is done in an electrolyte of Hanks' solution at a normal body temperature of ±37°C. Hanks' solution is a simulated body fluid which was prepared using high purity reagents. The composition of Hanks' solution is shown in Table 2.

Table 2 Chemical composition of Hanks' solution

COMPONENT	NaCl	$NaHCO_3$	$Na_2HPO_4.2H_2O$	KCl	KH_2PO_4
(g/L)	8.0	0.35	0.014	0.4	0.06
COMPONENT	$CaCl_2$	$MgSO_4.7H_2O$	$MgCl_2.6H_2O$	$C_6H_{12}O_6$	
(g/L)	0.14	0.06	0.1	1.0	

Corrosion behaviour was evaluated using Gamry Interface 1000 potentiostat and the experimental set-up is shown in Fig.9. The experimental set-up consists of a glass cell shown in Fig.10 which can contain 300 ml of electrolyte. The glass cell has a provision for inlet and outlet pipes which are connected to a water bath to allow circulation of water and maintain the temperature of the Hank's solution at ±37°C. A standard calomel electrode (SCE) is used as a reference electrode and a graphite rod as a counter electrode. Fig.11 shows the schematic arrangement of the electrochemical system.

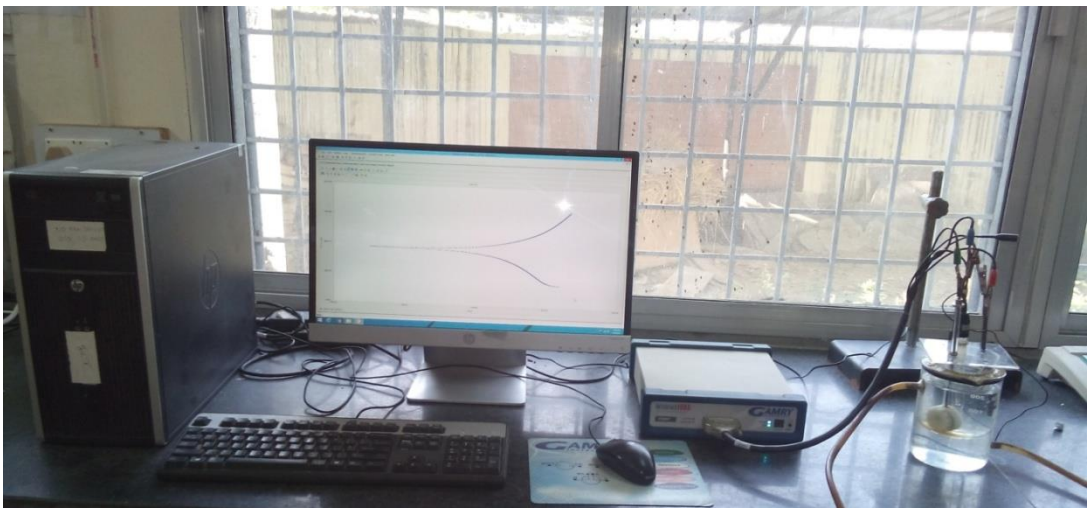

Fig.9. Experimental set-up to evaluate the corrosion behaviour

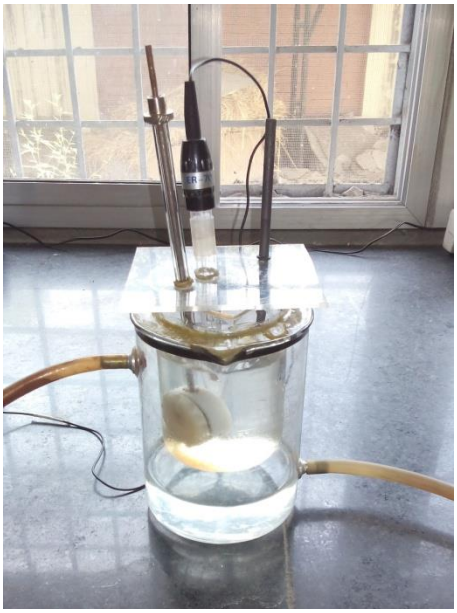

Fig.10. Glass cell with inlet and outlet for hot water circulation showing electrode positions

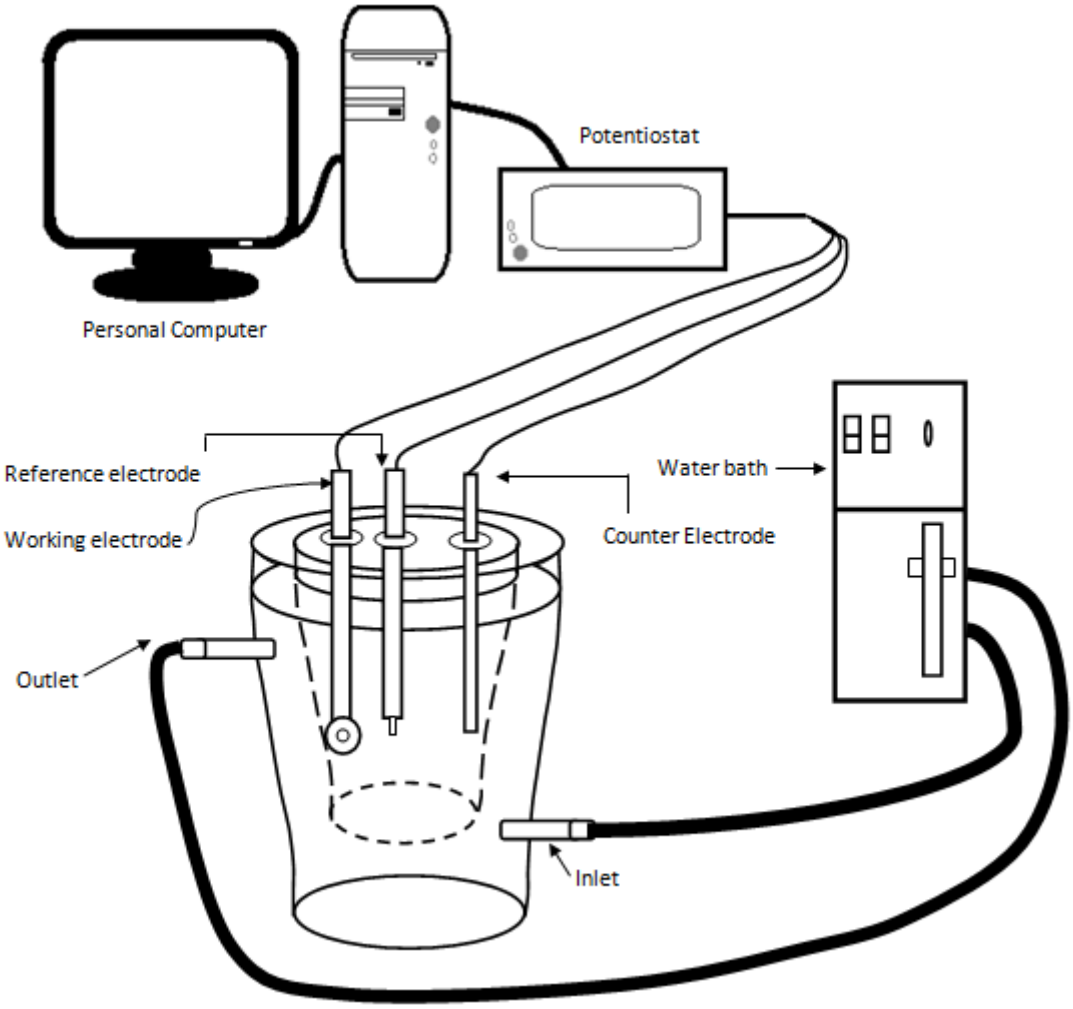

Fig.11. Schematic arrangement of corrosion test assembly

Samples of thickness around 3mm were cut so as to fulfil the requirements of the sample holder which has a 8mm diameter orifice, from which the sample gets exposed to the electrolyte. Now, the samples were successively polished using SiC emery paper starting from a grit size of 320, 800, 1200, and 1500, followed by cloth polishing with alumina. After cathodic treatment at −1.2V vs. SCE, samples were allowed to stabilize for 300 seconds when the open circuit potential (OCP) was determined. This is done to stabilize the system before testing.

Potentiodynamic Tafel testing was conducted for the as-received and all the MAFed samples of 316L SS in Hanks' solution from -250 mV to +250 mV range about the OCP at a scan rate of 1 mV/s. Cyclic polarization tests were performed in Hanks' solution with a forward and reverse scan rate of 1 mV/s and with a peak current density of 10 mA/cm^2 in order to ensure breakdown potential has been exceeded.

Also, the corrosion behaviour of the as-received and MAFed 316L SS samples were evaluated in Ringer's solution, which is an isotonic solution which simulates the body fluids of an animal. The chemical composition of Ringer's solution is shown in Table 3.

Table 3 Chemical composition of Ringer's solution

COMPONENT	NaCl	KCl	$CaCl_2$	Na_2CO_3
(g/L)	6.5	0.42	0.25	0.2

Potentiodynamic Tafel testing was performed in Ringer's solution from -250 mV to +250 mV range about OCP at a scan rate of 1 mV/s.

Apart from medical implants, UFG 316L stainless steel has a wide applicability in marine environments, food preparation equipment, jet engine components, power generation, etc,. Hence, its corrosion behaviour is evaluated in 3.5wt% NaCl solution at room temperature. Potentiodynamic Tafel testing was performed in 3.5wt% NaCl from −250 mV to +250 mV about OCP at a scan rate of 1 mV/s. Cyclic polarization tests were performed with a forward and reverse scan rate of 1 mV/s and with a peak current density of 20 mA/cm^2.

4.5. TRIBOCORROSION TESTING

The apparatus used in this study is shown in Fig.12**.** It consists of a Pyrex glass cell mounted on a pin-on- disc tribometer. This glass cell has a counterface fixed in its base with a standard epoxy adhesive of araldite. The glass cell can contain the electrolyte and is called as a tribo-electrochemical cell. The counterface is a 40 mm ceramic disc which is being characterised by energy dispersive spectroscopy (EDS) in the SEM. Also, the roughness of the counterface was characterised by using optical profilometry.

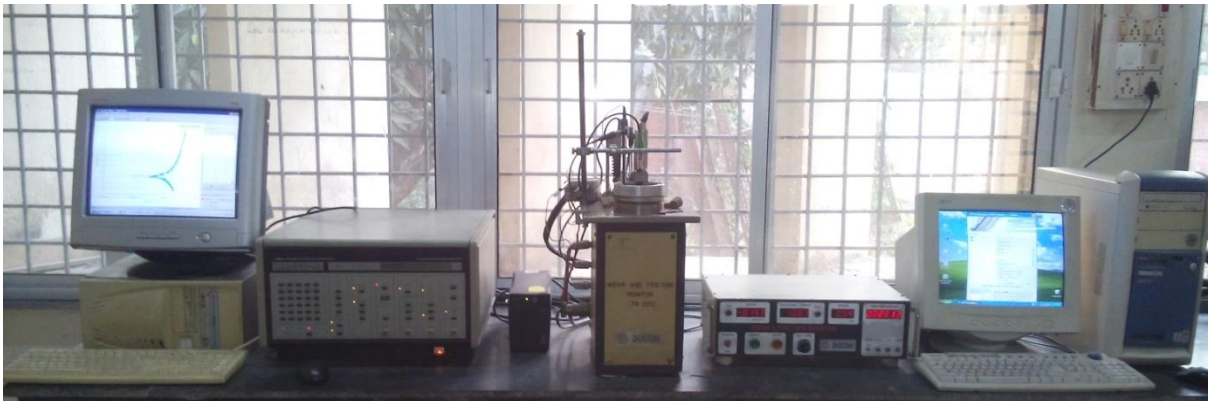

Fig.12. Experimental set-up to evaluate the tribocorrosion behaviour

The as-received and 3 pass and 12 pass MAFed samples of 316L SS were machined out as pin shaped samples to study the tribocorrosion behaviour. The pins have a diameter of 5 mm and a length of 10 mm as shown in Fig.13. The end surfaces of the pin samples were successively polished using SiC emery papers starting from 320, 800, 1200, and 1500 grit size to obtain a mirror-like surface.

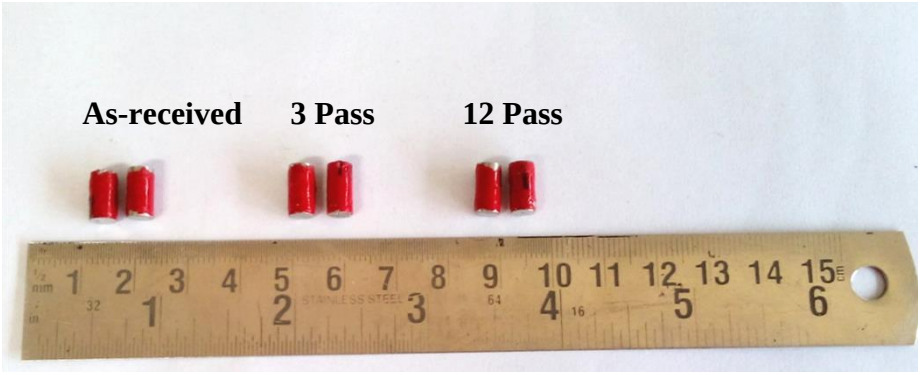

Fig.13. Pin samples of 316L SS used for tribocorrosion testing

The tribocorrosion experiments were conducted at room temperature in a simulated body fluid of Hanks' solution. The schematic arrangement is shown in Fig.14. A glass cell is used to contain about 50 ml electrolyte, SCE is used as a reference electrode, graphite rod as a counter electrode and Hanks' solution is used as an electrolyte.

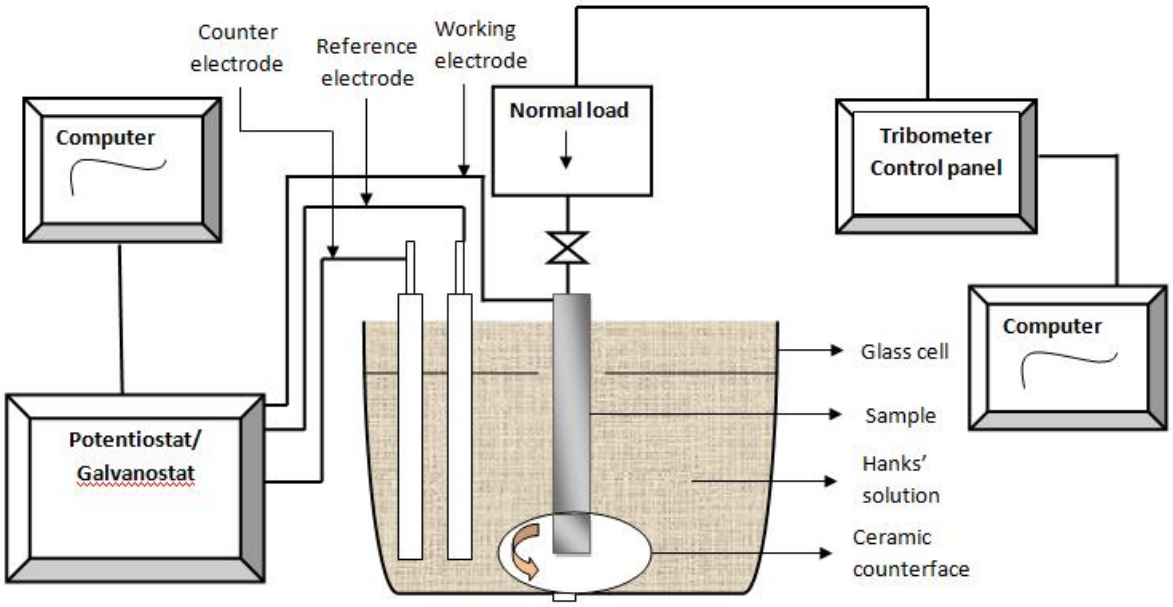

Fig.14. Schematic arrangement of tribocorrosion test assembly

A test area of 0.196 cm^2 of the pin sample base was made by insulating the rest of the surface with insulating adhesive nail paint. Now, the samples could be loaded into the tribo-electrochemical cell. The test area actually gets exposed to the electrolyte of Hanks' solution. During the test, a specimen holder was loaded with the stationary pin specimen vertically onto the rotating counterface. The normal load was applied via a lever mechanism and the tangential force due to friction i.e., frictional force was measured by the controller and recorded by the data acquisition system.

Sliding wear test at OCP was carried out using a Ducom-make pin-on-disc machine and the OCP was monitored using a potentiostat. Initial and final weights of the samples were recorded to calculate the wear volume. These sliding wear tests were performed at three contact normal loads of 10 N, 15 N, and 20N. The rotation speed of the disc and the test duration was maintained by the controller as 60 rpm and 5000 s respectively. Before sliding the specimen was stabilized at OCP under rotation-only condition for 300 s. OCP was continuously recorded by Powersuite® software. Also, the frictional force was recorded continuously which helped to determine the coefficient of friction (COF). All the samples were finally studied under SEM to characterize the wear surface.

Potentiodynamic polarization testing was done to measure the polarization curves of the as-received, 3 pass and 12 pass pin samples without sliding in Hanks' solution. It was done at a scan rate of 1 mV/s from a potential of −0.25 V vs. OCP to a potential of 1.2 V. Under the sliding condition, the sample was stabilized for 600 s i.e., the sample is allowed to slide over the counterface for 600 s, only after which the polarization curve was recorded. The polarization curve during sliding is measured under a contact load of 20 N and a rotation speed of 60 rpm. Under non-sliding condition, there is no contact between the specimen and the counterface but the specimen will be in contact with the electrolyte in glass cell that is rotating at a speed of 60 rpm. Before each polarization measurement, the specimen was stabilised at OCP for 300 s. For a particular condition of a sample, the polarization curves during sliding and without sliding were measured and compared.

CHAPTER 5: RESULTS AND DISCUSSION

5.1. WARM MULTI-AXIALLY FORGED 316L

The as-received 316L SS samples were warm multi-axially forged with a strain of -0.4 per pass for 3, 6, 9, and 12 passes. The forged samples are shown in Fig.15.

Fig.15. Warm multi-axially forged 316L SS samples of as-received, 3 pass, 6 pass, 9 pass, and 12 pass conditions

The samples retained their shape and dimensions even after 12 passes of MAF i.e., there is no or negligible distortion in the samples.

5.2. MICROSTRUCTURAL CHARACTERISATION

5.2.1. XRD ANALYSIS

Martensite formation needs to be avoided as it negatively affects the corrosion behaviour. The safe working range is therefore around 630°C i.e., (<0.5 T_m) that hinders martensite formation. This is further confirmed from XRD data, where the XRD peaks correspond to austenite phase only after 3, 6, 9, and 12 passes of forging as shown in Fig.16. The percentage of other phases formed, if any, is only less than 5% of the total volume. Also from Fig.16, it is clear that there is no change in peak position among the samples which represents there is less or negligible residual stress in the sample after MAF.

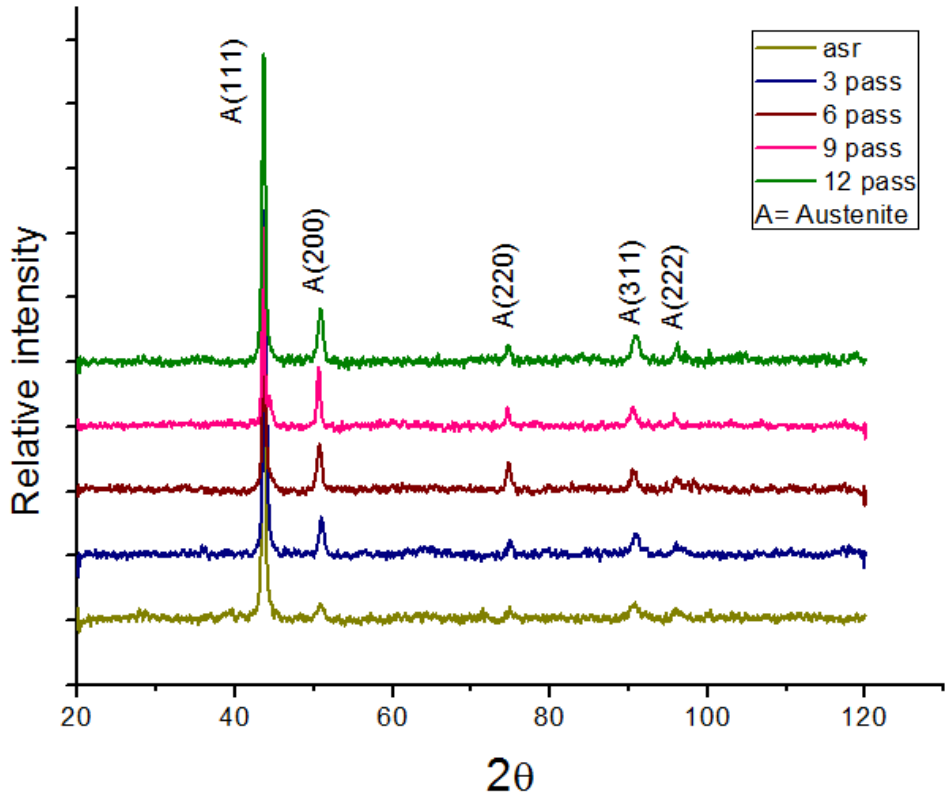

Fig.16. XRD patterns of as-received, 3, 6, 9, and 12 MAF pass samples of 316L SS showing a completely austenitic structure

5.2.2. OPTICAL MICROSCOPY

Figs.17 (a), (b), (c), (d), and (e) show the optical micrographs of as-received, 3, 6, 9, and12 pass MAFed samples, respectively. With an increase in the number of MAF passes, there is increased grain refinement. Nevertheless, due to the low range of magnifications in the optical microscope and high degree of grain refinement in the samples, the visibility of grains and grain boundaries is not clear. Hence, the samples were further observed using the SEM for a better understanding of the grain refinement.

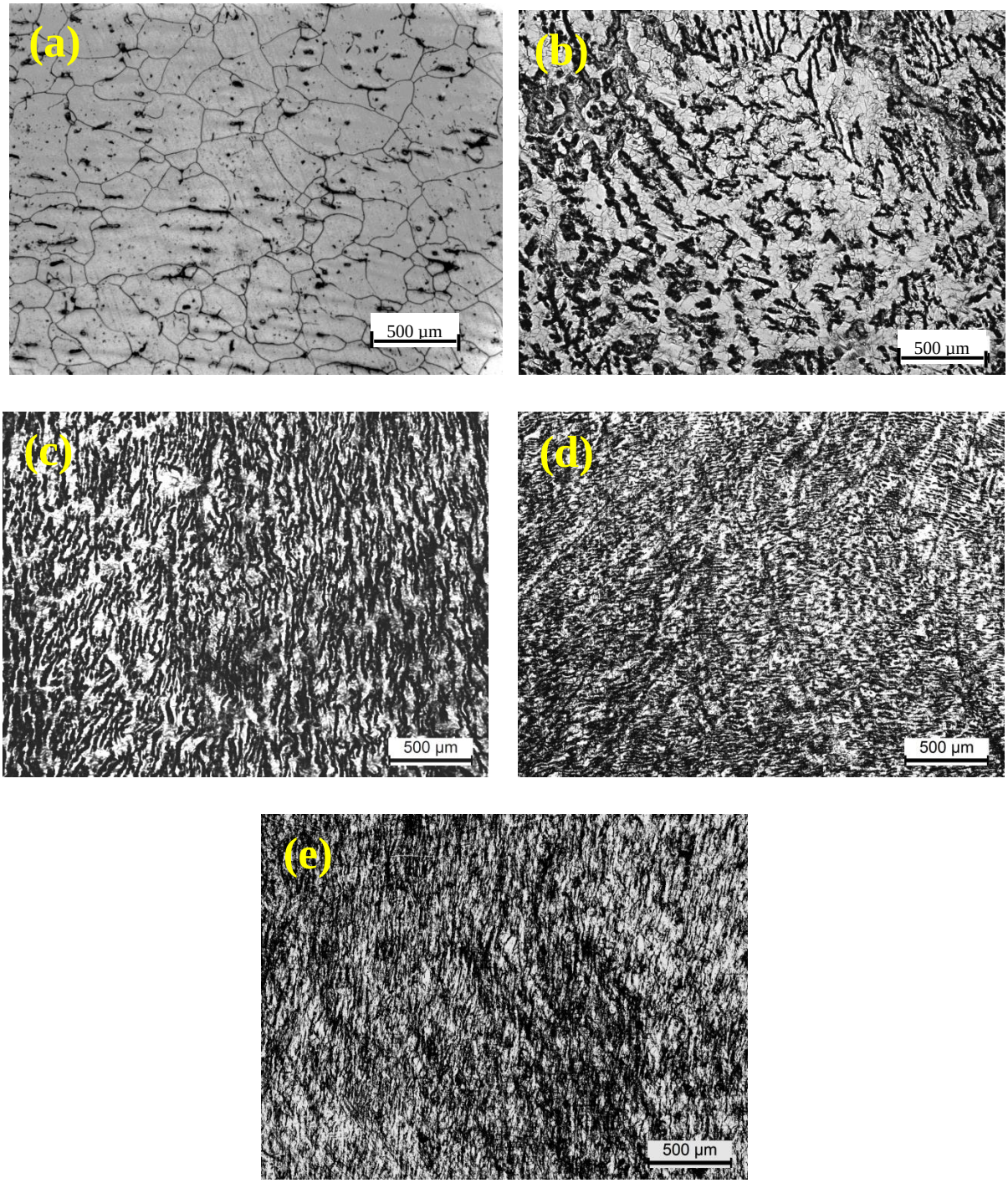

Fig.17. Optical micrographs of 316L SS in (a) as-received condition, and after warm MAF at 630°C using (b) 3, (c) 6, (d) 9, and (e) 12 passes

5.2.3. SEM ANALYSIS

The SEM micrograph of the as-received 316L SS is shown in Fig.18 (a). Using linear intercept method, the average grain size of the as-received material is estimated as 55 µm.

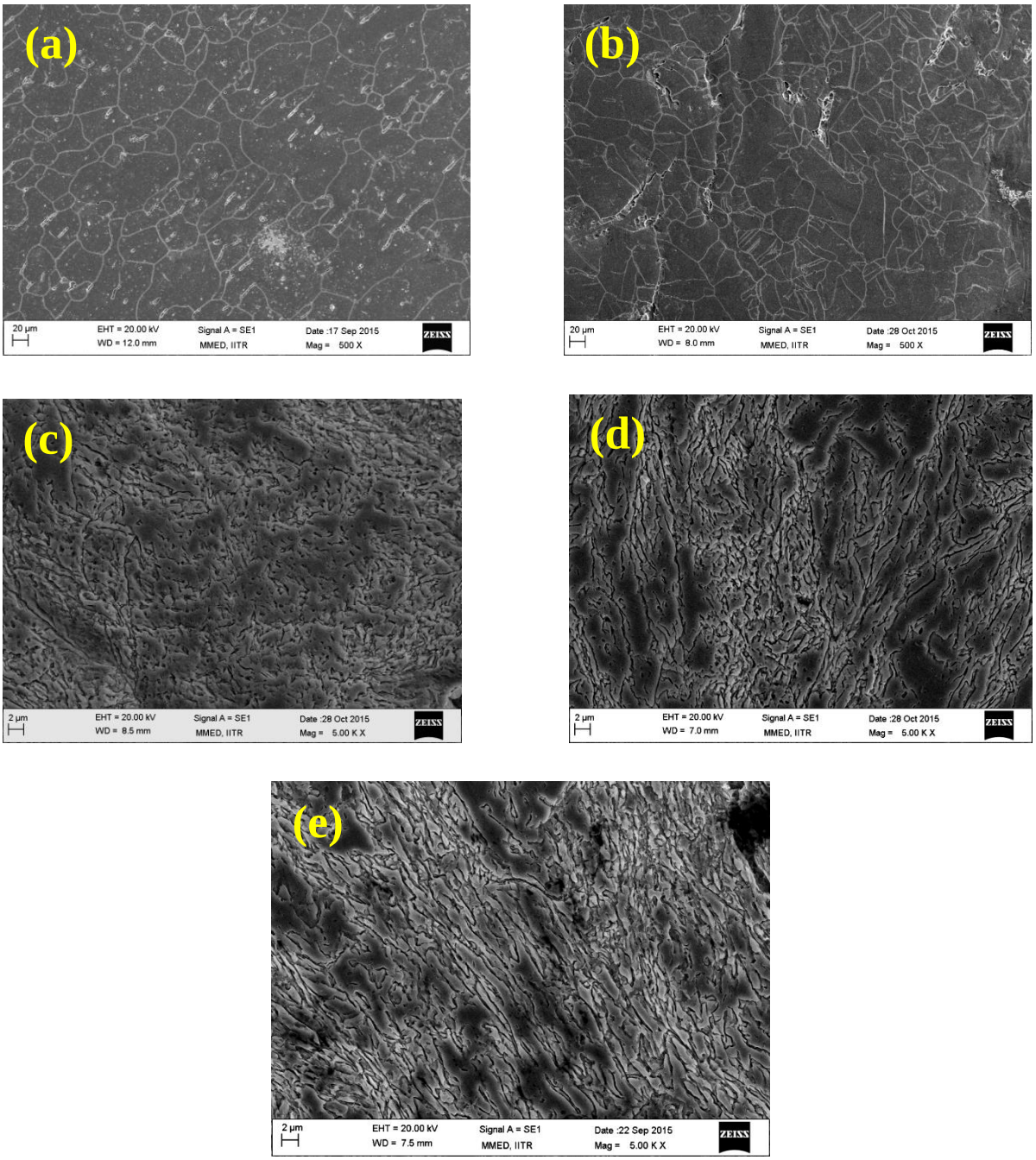

Fig.18. SEM micrographs of 316L SS in (a) as-received condition, and after MAF at 630°C using (b) 3, (c) 6, (d) 9, and (e) 12 passes

Figs.18 (b), (c), (d), and (e) show the SEM micrographs of 3, 6, 9, and 12 MAF pass samples, respectively. The 3 pass MAF sample does not show much refinement, whereas 6 pass, 9 pass, and 12 pass MAF samples showed a significant grain refinement. Patterns of etch pits can be seen in the SEM micrographs inside the grains confirming a high dislocation density within the grains. The 6 pass and 9 pass samples showed formation of sub-structures within the grains as shown in Fig.18 (c) and (d). For the 12 pass sample, a bimodal grain structure consisting of ultra-fine grains and large grains is observed as shown in Fig.18 (e), thus suggesting the refinement mechanism of warm MAF as cDRX at higher strain steps. The material thus can achieve its strength from the ultra-fine grains and ductility from the coarse grains [28]. This may be further confirmed by electron back scattered analysis.

5.2.4. TEM ANALYSIS

Bright field TEM images of the MAFed using 3, 6, 9, and 12 passes of 316L SS are shown in Fig.19**.** From the Fig.19, it is evident that as the number of MAF passes increase, the dislocation density increases which makes the austenite grains sub-divide into "cells". These cells have a random orientation which can be understood from the diffraction rings of selected area electron diffraction pattern (SAED).

Fig.19 (a) shows the bright field TEM micrograph of 3 pass MAFed 316L SS, where the initiation of the initial dislocation sub-structure is observed. Thus, it is clear that at the initial passes of MAF, substructures develop within the initial austenite grains. Hence, the SAED pattern shown in Fig.19 (b) represents no or negligible misorientation in the particular specimen area.

Fig.19 (c) shows the bright field TEM micrograph of the 6 pass sample, where the grains contained high dislocation density and thus creating finer sub-grains within the original grains. This is confirmed from the SAED pattern in Fig.19 (d) where the degree of misorientation has comparatively been increased.

The 9 pass MAFed sample has moderate dislocation density inside the grains while the grain boundaries that are yet to be developed have a high dislocation density as shown in Fig.19 (e). Also, there is a combination of grains with dislocations and dislocations-free grains. This represents that at high strains, grain boundaries are in non-equilibrium condition.

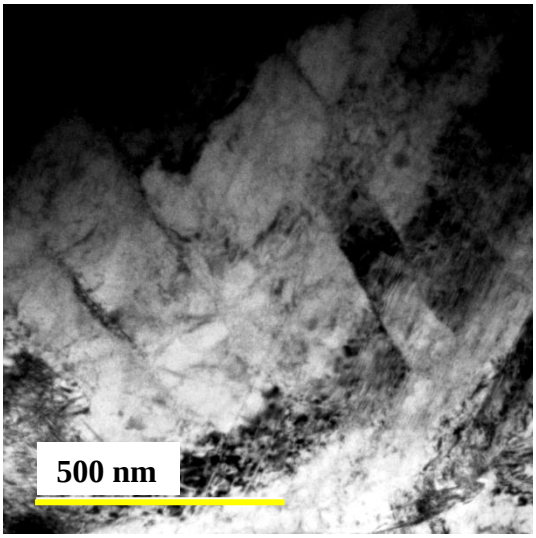
500 nm

(a)

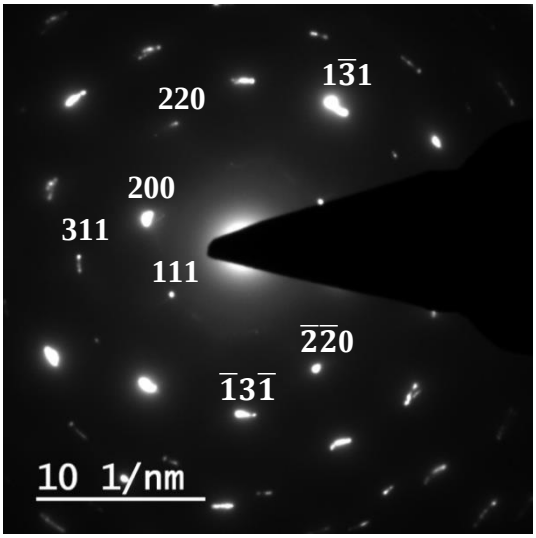
220
1$\bar{3}$1
200
311
111
$\bar{2}\bar{2}$0
$\bar{1}3\bar{1}$
10 1/nm

(b)

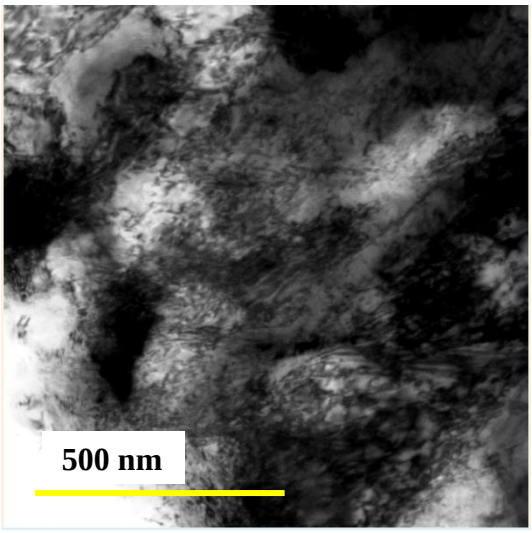
500 nm

(c)

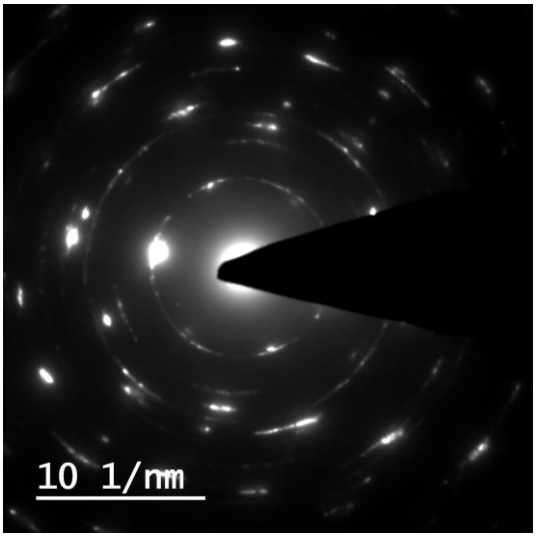
10 1/nm

(d)

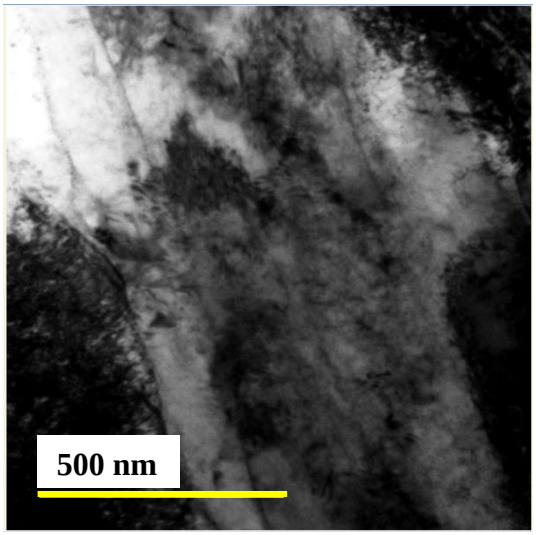
500 nm

(e)

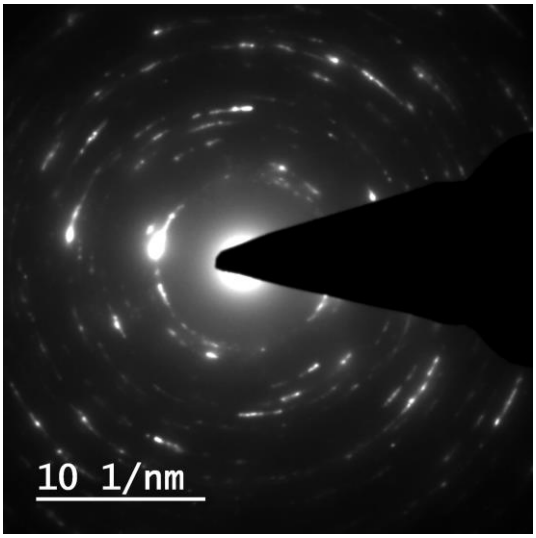
10 1/nm

(f)

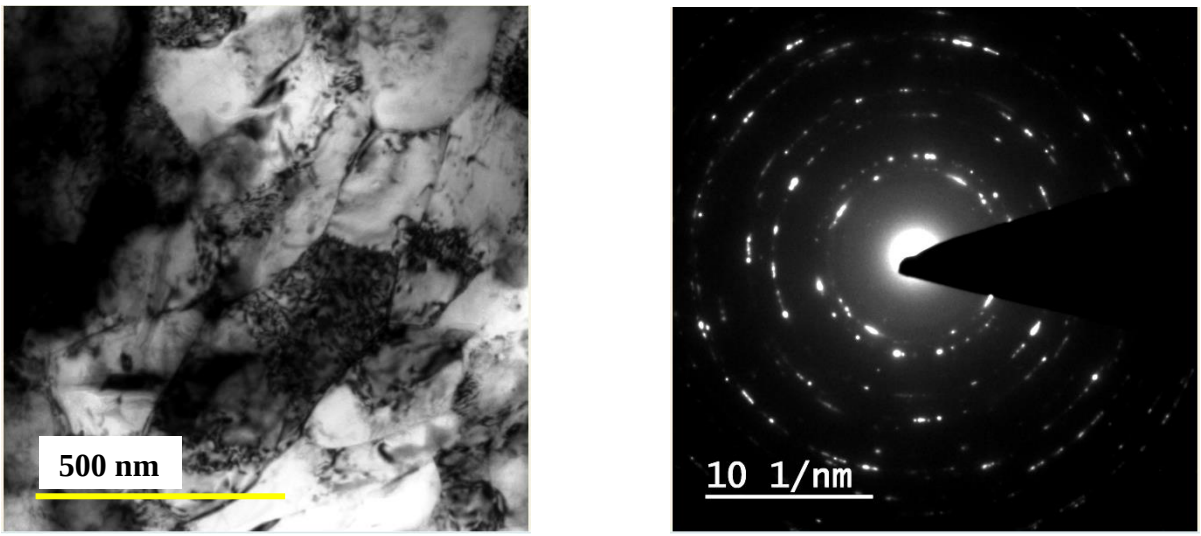

(g) (h)

Fig.19. TEM micrographs and SAED patterns of (a), (b) 3 pass, (c), (d) 6 pass, (e), (f) 9 pass, and (g), (h) 12 pass MAFed 316L SS samples respectively

The 12 pass TEM micrograph is shown in Fig.19 (g). The dislocation density is substantially reduced inside the grains while there is still a high dislocation density along the grain boundaries. As a result, fine grains were formed with high angle boundaries. It is apparently the cDRX process that is making the dislocations get absorbed at the grain boundaries. From the SAED pattern shown in Fig.19 (h), it is evident there is a large degree of misorientation between the grains which points to a highly refined grain size. As the grains and grain boundaries are comparatively clear, the average grain size is calculated using linear intercept method. The average grain size of the 12 pass MAFed 316L SS is about 151.20 nm which is an evident for the UFG structure.

5.3. HARDNESS

The variation of Vickers hardness with the number of MAF passes is shown in Fig. 20. As can be seen, there is a drastic increase in the hardness till 3 MAF passes which is explained by strain hardening. Thereafter the hardness increases at a lower rate. As the number of passes increased, there is a reduction in dislocation density inside the grains as observed under TEM, leading to the softening of the material. Also, with the increase in number of MAF passes there is strengthening of the material due to the grain refinement. Hence, the competition between softening and strengthening makes the hardness increase at a lower rate at higher MAF passes [15]. The increase in hardness can also be attributed to the Hall-Petch strengthening resulting from grain refinement.

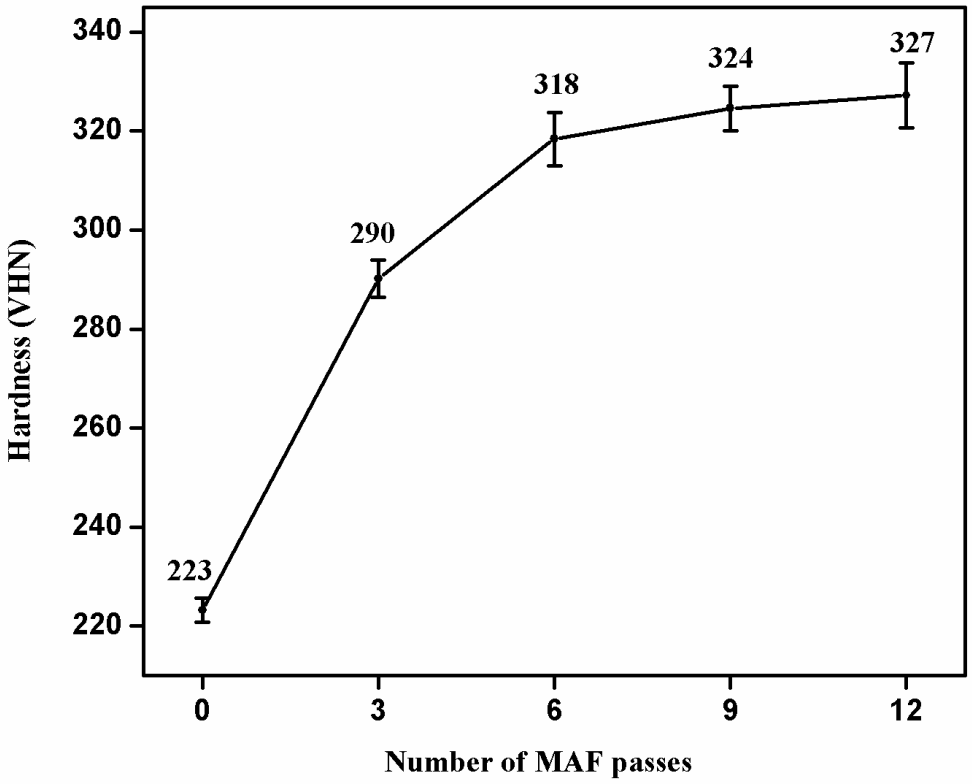

Fig.20. Hardness of different conditions of MAFed 316L stainless steel

5.4. CORROSION BEHAVIOUR

5.4.1. POTENTIODYNAMIC TAFEL BEHAVIOUR

Potentiodynamic Tafel tests were conducted to understand the uniform corrosion behaviour and to estimate the corrosion rate of the as-received and MAFed 316L SS. Initially the samples were stabilized about the OCP for 300 s. Fig. 21, 22, and 23 show the results of Tafel polarization tests of the as-received and MAFed samples, performed in Hanks' solution at body temperature of ±37°C, 3.5wt% NaCl solution at room temperature and Ringers solution at room temperature, respectively. Their corrosion potential (E_{corr}) and corrosion current (I_{corr}) are obtained by extrapolating the anodic and cathodic polarization regions and these are summarized in tables 4, 5, and 6 respectively**.** Corrosion rate is calculated using the formula stated in ASTM standard [29] that is given by equation (2).

$$\mathrm{CR} = 3.27 \times 10^{-3} \times \frac{I_{\mathrm{corr}} \times \mathrm{Equivalent\ weight}}{\mathrm{Density}} \qquad (2)$$

Where,

I_{corr} in µA cm^{-2} is obtained by the extrapolation of cathodic and anodic polarisation curve. Equivalent weight of 316L SS is 25.227 g and density of 316L SS is 7.763 g cm^{-3}.

Almost all the MAFed samples exhibit the similar anodic polarization behaviour as shown in the Fig. 21, 22, and 23. Irrespective of the electrolyte, the OCP values of the MAFed samples shifted slightly to more negative values when compared to the as-received 316L SS sample. This is may be due to the competition between less or negligible presence of residual stresses and increment of grain boundary volume pertaining from grain refinement.

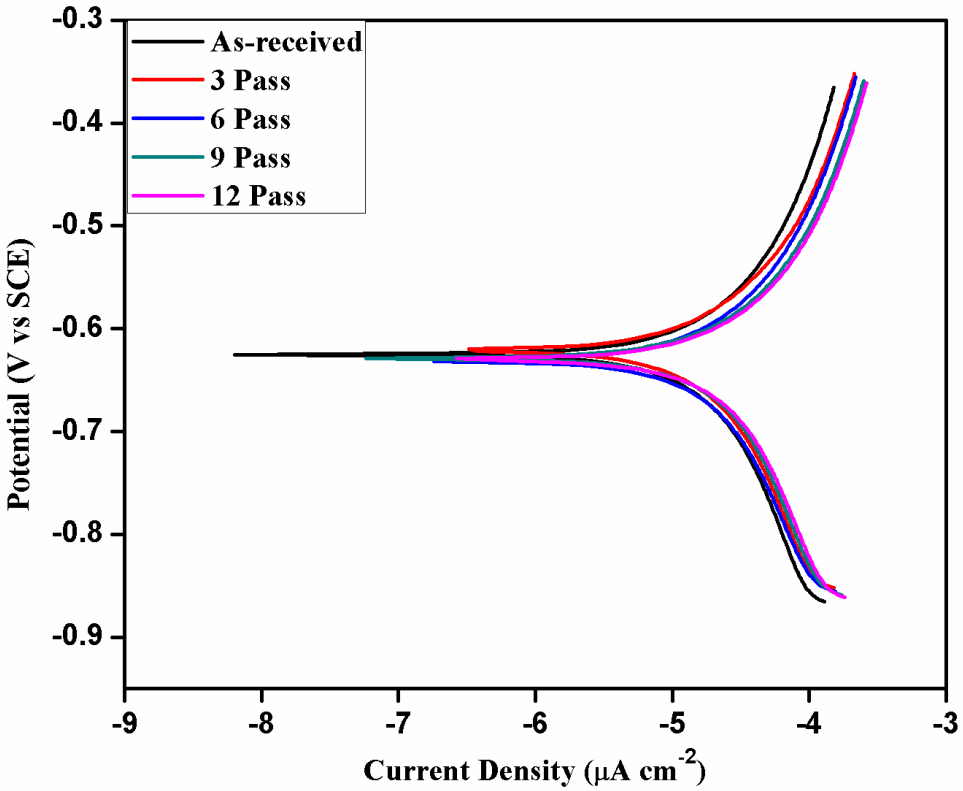

Fig.21. Comparative potentiodynamic Tafel behaviour of the as-received and MAFed 316L SS samples in Hanks' solution at 37°C

Table 4 Results of Tafel polarization test performed in Hanks' solution at 37°C

Sample of 316L SS	**E_{corr} (mV vs. SCE)**	**I_{corr} (μA cm^{-2})**	**Corrosion rate (mm $year^{-1}$)**
As-received	−621	4.56	0.0489
3 Pass	−624	4.60	0.0489
6 Pass	−627	4.62	0.0490
9 Pass	−628	4.65	0.0494
12 Pass	−630	4.67	0.0496

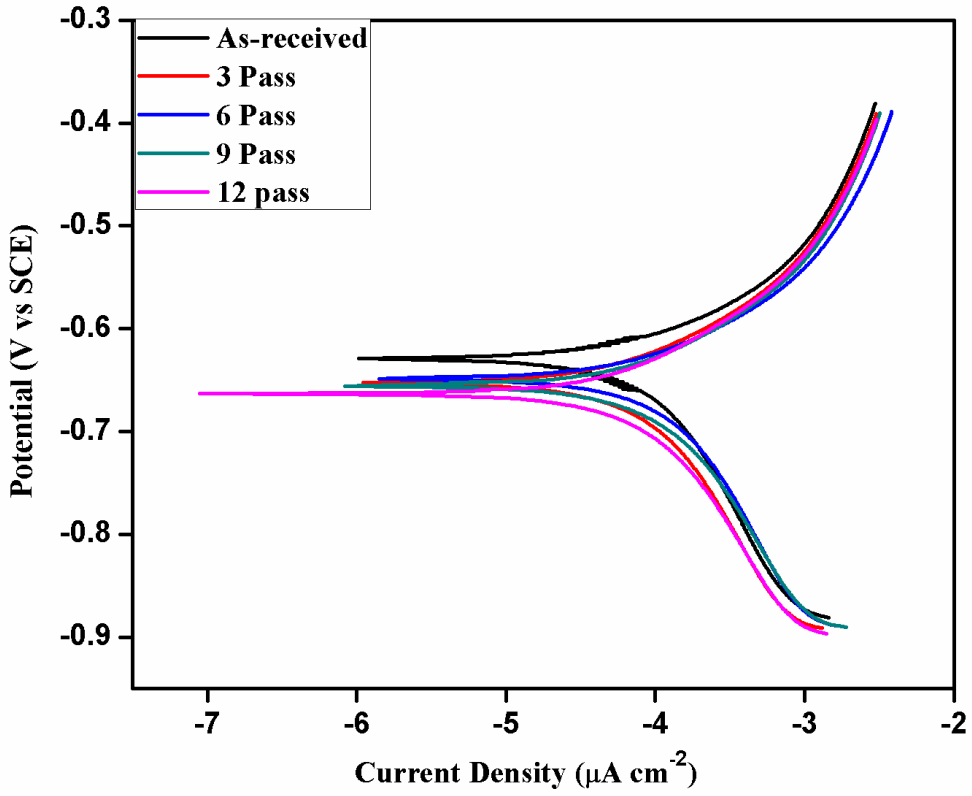

Fig.22. Comparative potentiodynamic Tafel behaviour of the as-received and MAFed 316L SS samples in 3.5 wt% NaCl solution at room temperature

Table 5 Results of Tafel polarization test performed in 3.5 wt% NaCl solution at room temperature

Sample of 316L SS	**E_{corr} (mV vs. SCE)**	**I_{corr} (μA cm^{-2})**	**Corrosion rate (mm $year^{-1}$)**
As-received	-629	3.84	0.0408
3 Pass	-651	3.87	0.0411
6 Pass	-653	3.90	0.0414
9 Pass	-657	3.93	0.0418
12 Pass	-661	3.99	0.0424

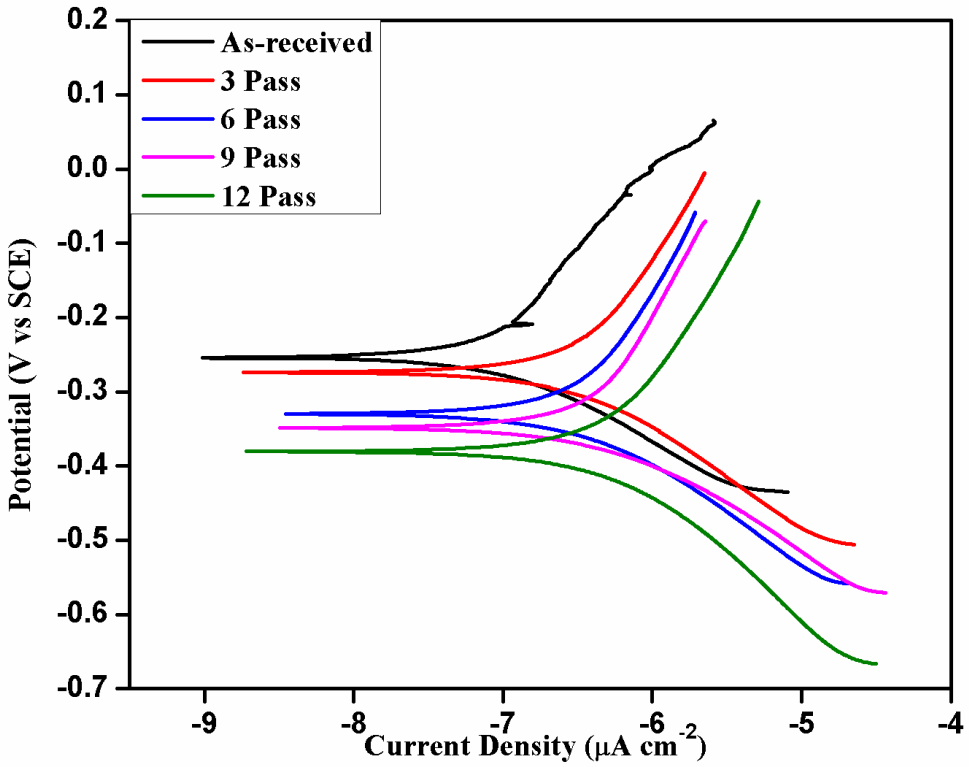

Fig.23. Comparative potentiodynamic Tafel behaviour of the as-received and MAFed samples in Ringer's solution at room temperature

Table 6 Results of Tafel polarization test performed in Ringer's solution at room temperature

Sample of 316L SS	**E_{corr} (mV vs. SCE)**	**I_{corr} (μA cm^{-2})**	**Corrosion rate (mm $year^{-1}$)**
As-received	-250	6.21	0.0660
3 Pass	-274	6.40	0.0680
6 Pass	-327	6.52	0.0693
9 Pass	-348	6.81	0.0724
12 Pass	-381	7.07	0.0751

From the Tables 4, 5, and 6, it is observed that the corrosion potential is becoming more negative and the corrosion current density is increasing as the number of MAF passes increased. The reason behind this variation is, as the number of MAF passes increase, there is a subsequent grain refinement providing with large grain boundary volume. These large numbers of grain boundaries are the sites of internal stored energy which makes possible to increases the anodic reaction rate and hence making the E_{corr} more negative when the number of passes is increased.

One of the factors that affect corrosion behaviour is the type of electrolyte. When the corrosion rates of the as-received and MAFed samples in different electrolytes of Hanks' solution, 3.5 wt% NaCl solution and Ringer's solution are compared, it is observed that the samples exhibited a better and lower corrosion rate in 3.5 wt% NaCl solution. Also, in the case of Tafel test in Hanks' solution and 3.5wt% NaCl solution for different samples, the change in E_{corr} and I_{corr} is very less, indicating that the uniform corrosion behaviour of the material is unaffected even after MAF.

5.4.2. CYCLIC POLARIZATION

Cyclic polarization gives an idea about the anodic and cathodic polarization behaviour in a cyclic manner. It is used to measure the pitting corrosion tendency of a material in a particular electrolyte. It provides information about the formation of a passive film, its breakdown and further repassivation after which there is no new pitting. Thus, pitting corrosion resistance of a material depends on the,

1. ability to form a passive film,
2. potential at which the film breaks,
3. ability to repassivate, and
4. area enclosed by the loop

During anodic polarization, the potential after which there is a sudden increase in current density is termed as breakdown potential (E_{bd}) or pitting potential. This sudden increase in current density is due to the breakdown of passive film and thereby making the surface active. The curve reverses and completes a cycle by intersecting the anodic curve, called as the repassivation potential (E_{rp}). The presence of a loop is an indicative of pitting in the

material while the area of the loop decides the amount of pitting. A higher value of E_{bd}, E_{rp} and a smaller area enclosed by the loop are desirable for good localized corrosion resistance. Cyclic polarization curves of the as-received, 3 pass, and 12 pass MAFed 316L SS samples in Hanks' solution are shown in Fig.24.

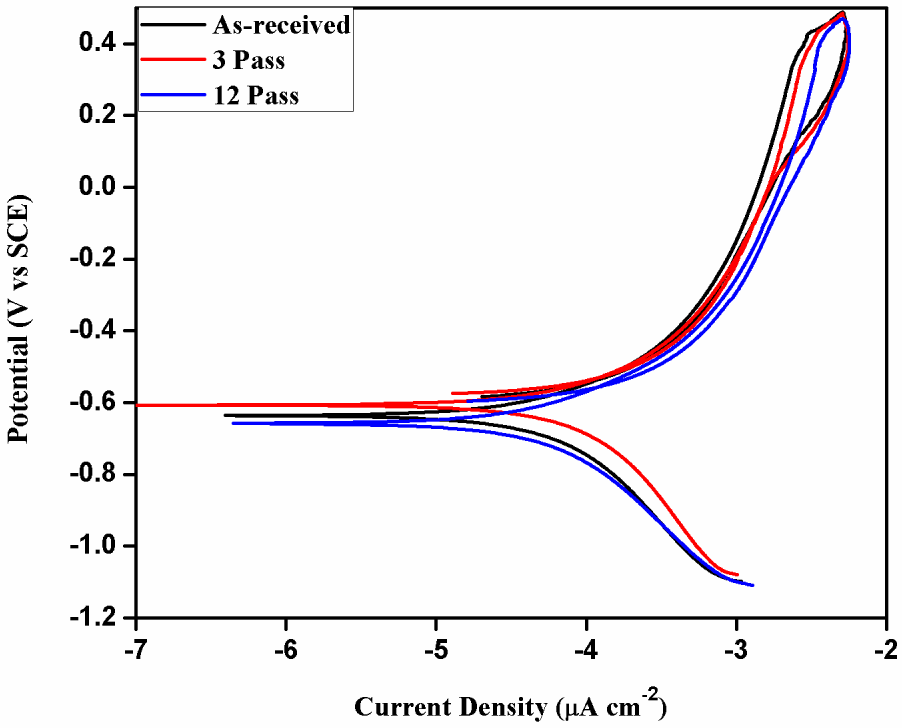

Fig.24. Comparative cyclic polarization behaviour of the as-received and MAFed samples in Hanks' solution at 37°C

Table 7 Results of cyclic polarization test in Hanks' solution at 37°C

Sample of 316L SS	E_{bd} (mV vs. SCE)	E_{rp} (mV vs. SCE)
As-received	317	-543
3 Pass	325	-537
12 Pass	332	-538

From Fig.24, it is observed that there is an increase in the passive range in Hanks' solution with the increase in number of MAF passes. Hence, there is a shift in the E_{bd} to more positive potentials with the number of MAF passes as shown in Table 7. In addition, the 12 pass sample has the least area under the loop, which is one of the deciding factors of pitting susceptibility. There is no much difference in the repassivation potentials of the as-received and 12 pass sample, thus proving that the 12 pass MAFed sample has better pitting corrosion resistance in Hanks' solution. This may be attributed to the combined effect of increase in grain boundary volume and homogenization of pit-inducing impurities and non-metallic phases due to SPD [30].

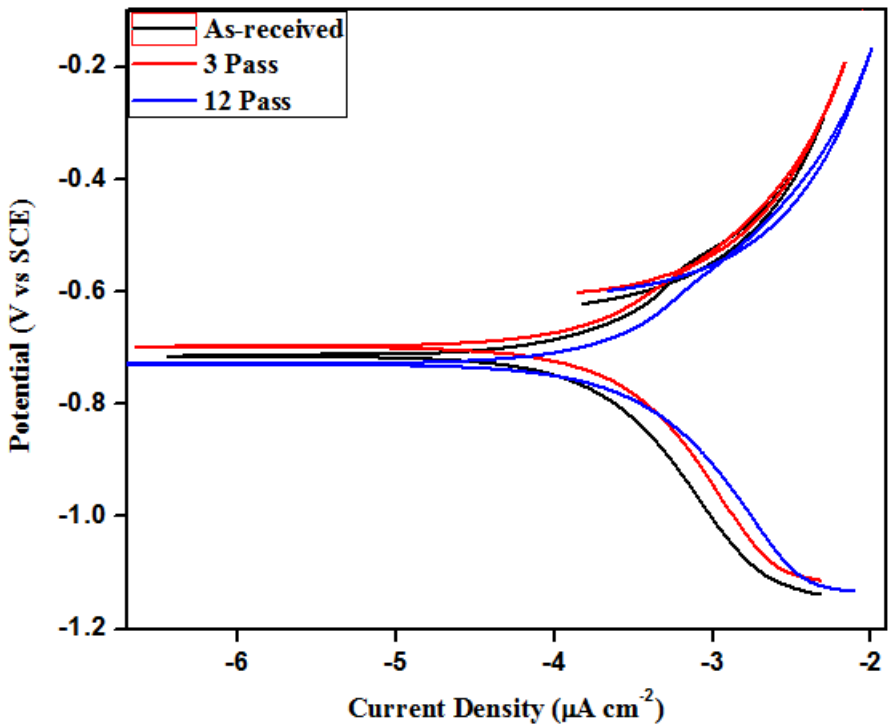

Fig.25. Comparative cyclic polarization behaviour of the as-received and MAFed samples in 3.5 wt% NaCl solution at room temperature

Fig.25 shows the results of cyclic polarisation test of the as-received and MAFed 316L SS in 3.5wt% NaCl solution at room temperature. From the Fig.25, it is seen that a sharp cyclic loop is obtained in 3.5wt% NaCl solution for the as-received and MAFed samples, which

shows no breakdown potential. Also, there is no loop which indicates that the sample remains passive i.e., no pits were formed in 3.5wt% NaCl solution. Hence, it is proved that MAF has no effect on pitting corrosion behaviour of 316L SS in 3.5wt% NaCl solution.

5.5. TRIBOCORROSION CHARACTERIZATION

5.5.1. CHARACTERIZATION OF THE COUNTERFACE

Pin-on-disc type set-up is used to investigate the tribocorrosion behaviour of 316L SS. Here, the counterface used is a ceramic disc of 40 mm diameter. The composition of the counterface is characterised by EDS in the SEM, through which it is confirmed that the disc is an alumina based ceramic material. A SEM micrograph shown in Fig.26 (a) and the elemental composition shown in Fig.26 (b) is used to estimate the composition of the ceramic disc.

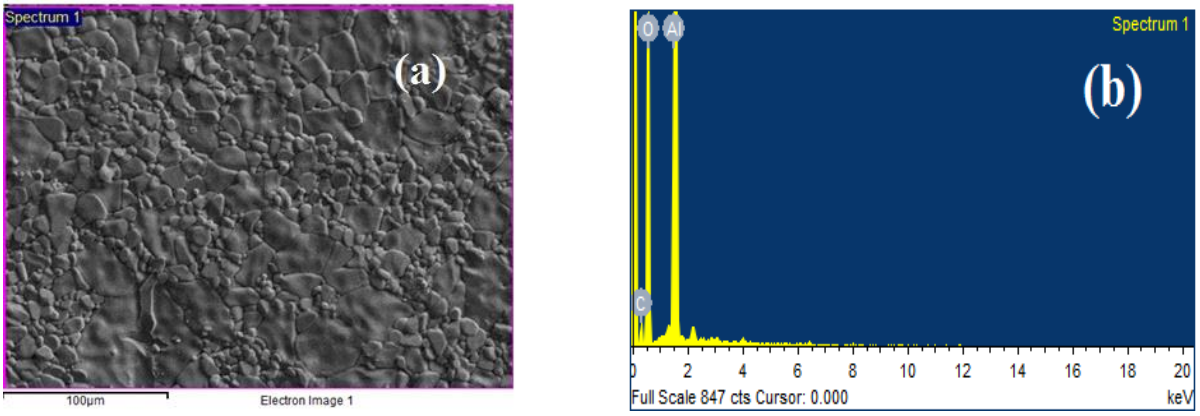

Fig.26. (a) SEM micrograph and (b) EDS spectrum of the counterface ceramic disc

The composition of the ceramic disc is thus found as 40.14 weight% of aluminium and 49.08 weight% of oxygen, hence showing that the ceramic disc is made up of alumina. In addition, the roughness of the counterface was characterised by using optical profilometry. From Fig.27, it is evident that the alumina disc has an average roughness of 2.3 µm.

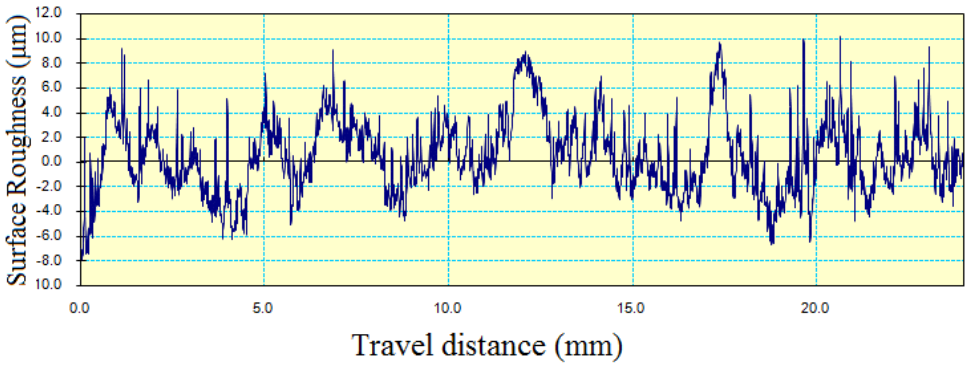

Fig.27. Graph showing the variation of surface roughness with travel distance on the alumina disc which is used as a counterface in the pin-on-disc tribocorrosion setup

5.5.2. SLIDING TESTS AT OCP

5.5.2.1. Effect of normal load on OCP

Sliding tests in Hanks' solution at the open circuit potential (OCP) were performed with three different contact loads of 10 N, 15 N and 20 N. Samples of 316L SS are covered by a passive film when they are placed in Hanks' solution. The OCP obtained during tribocorrosion is a combination of potentials of both the worn surface which becomes active and the unworn surface which is comparatively in passive condition [31]. The unworn surface appears as a result of improper contact with the counterface due to the random presence of asperities. Characteristic OCP curves obtained during the test are shown in Fig.28.

From Fig.28 (a), (b), and (c), it is evident that as soon as the sliding of the pin sample against the counterface starts, there is a sharp decrease in the OCP value towards the more negative potentials. This is due to the deterioration of the passive film at the contact area. The damaged surface at the contact area becomes active and there is a galvanic couple created between the active and passive regions [23]. As a result, the active area undergoes a quick local dissolution. And as it is known that the potential of an active surface is more negative when compared to a passive surface, hence, the OCP value shifts towards more negative value soon after the sliding is started. The OCP almost remains the same during the friction phase because of the counteraction of breakdown of the passive film and simultaneous repassivation.

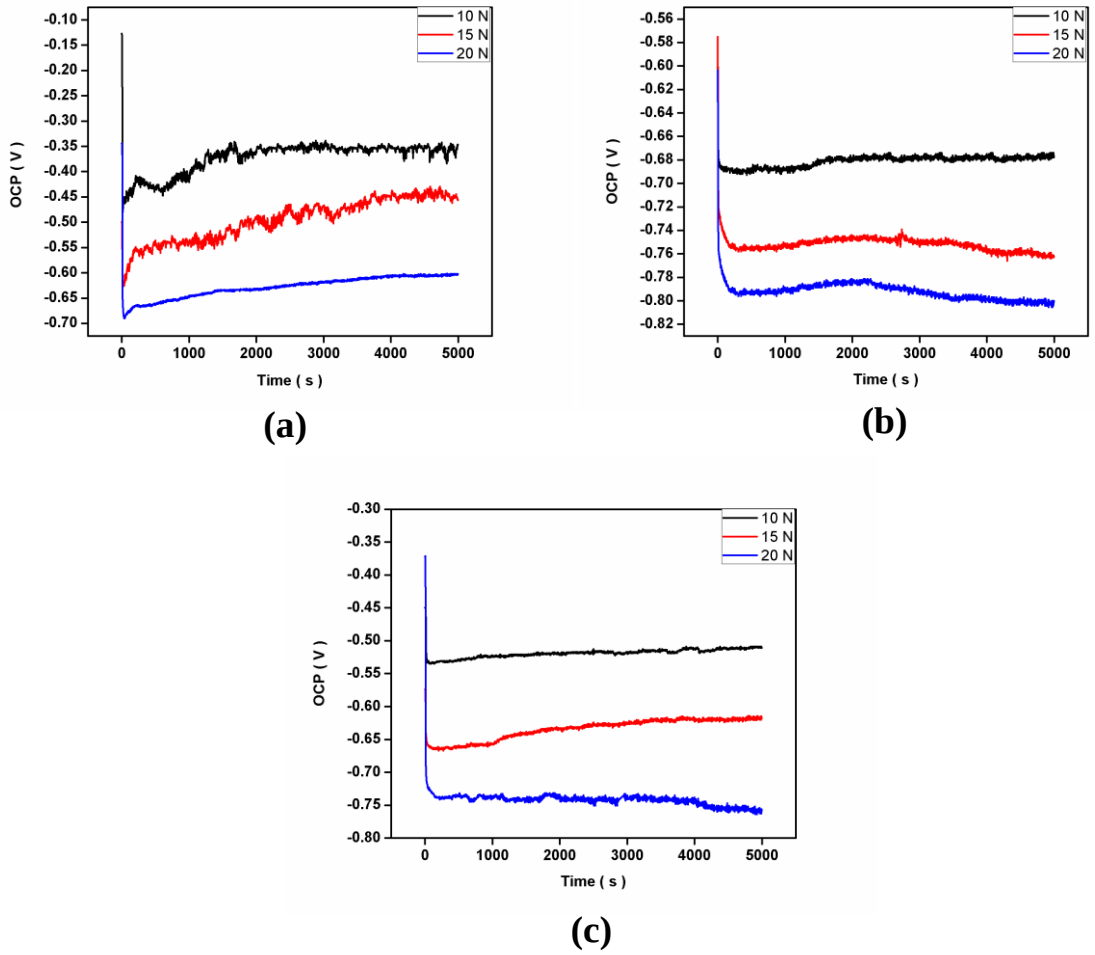

Fig.28. OCP values obtained at different contact loads of 10 N, 15 N, and 20 N for (a) as-received, (b) 3 pass, and (c) 12 pass samples in Hanks' solution

For the same condition of material, with the increasing load, there is a shift of OCP values towards more negative potentials as shown in Fig.28 (a), (b), and (c). This is because, as the load increases, the degree of deterioration of the passive film from the material surface increases. And there is a heavy competition between the formation and deterioration of the passive films, in which the deterioration property is highly dominated as the contact pressure is more at high loads. So, there is a drop in the OCP value as the load on the material increases. OCP thus is strongly dependent on the amount of worn area: the larger is the amount of worn area, the smaller is the OCP i.e., it becomes more active, because of the depassivation of the worn area.

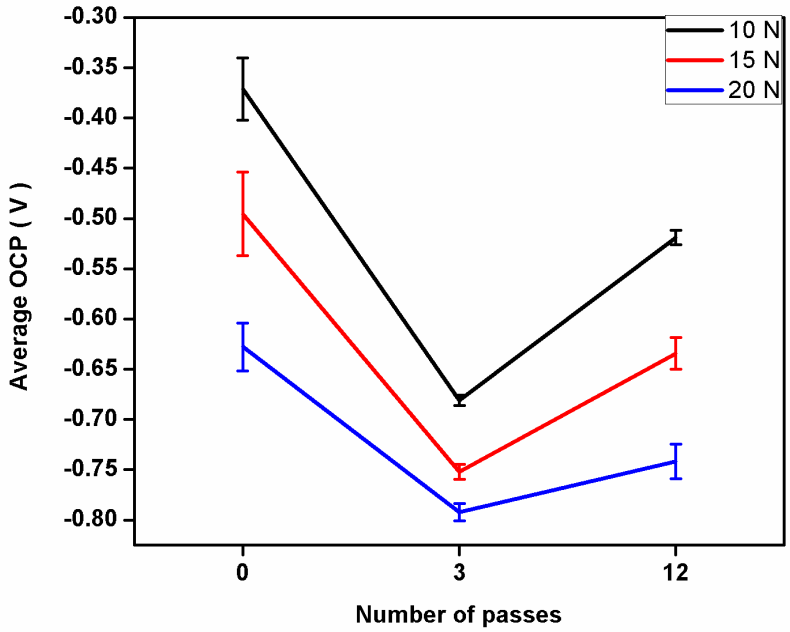

Fig.29. Average OCP values for different MAF passes

From Fig.29**,** it is observed that there is a decrease in OCP value of the 3 pass MAFed sample to more negative potentials. This is due to the reason that the 3 pass sample has still coarse grains with high dislocation density within the grains. As dislocations are a source of defects that can easily become active, the OCP value of the 3 pass sample becomes more negative suddenly. But for the 12 pass sample, there is a comparative rise of the OCP value which is due to the ultra-fine grained structure with lower dislocation density.

5.5.2.2. Effect of normal load on COF

Coefficient of friction is a value that relates the frictional force and the normal load between the pin sample and the counterface during sliding. Characteristic curves obtained during the sliding tests are shown in Fig.30.

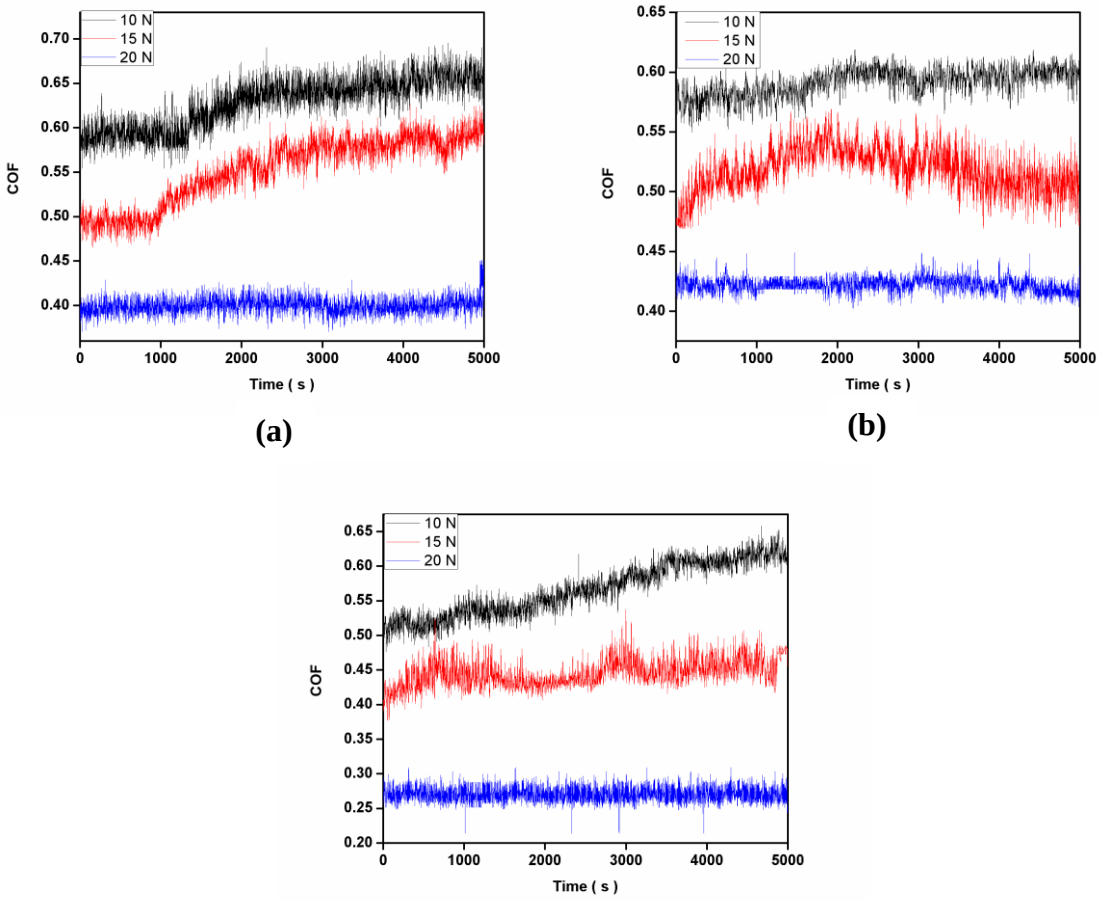

Fig.30. COF values obtained at different contact loads of 10 N, 15 N, and 20 N for (a) as-received, (b) 3 pass, (c) 12 pass samples respectively in Hanks' solution

From the Fig.30 (a), (b), and (c), it is evident that with increasing load, there is a decrease in the COF for all the different condition samples. At lower loads, the contact pressure is not sufficient to break the asperity contacts between the sample and counterface making it difficult for the sample to slide over the counterface. So, there is a higher value of COF observed. As the load is increasing, the tendency to wear off increases which makes the surface smooth by reducing the mechanical interlocking between surface asperities and the counterface. Thus, at higher loads there is a lower value of COF. Similar observations were made by Ahmad et al [32].

Also at highest load, the passive film breaks easily and the ability of repassivating is difficult. Hence, the COF has almost the same value with time, because there is a maximum area of metal surface which is in direct contact with the counterface. But at lower loads, the ability to repassivate prevails which makes the COF increase slightly with the time.

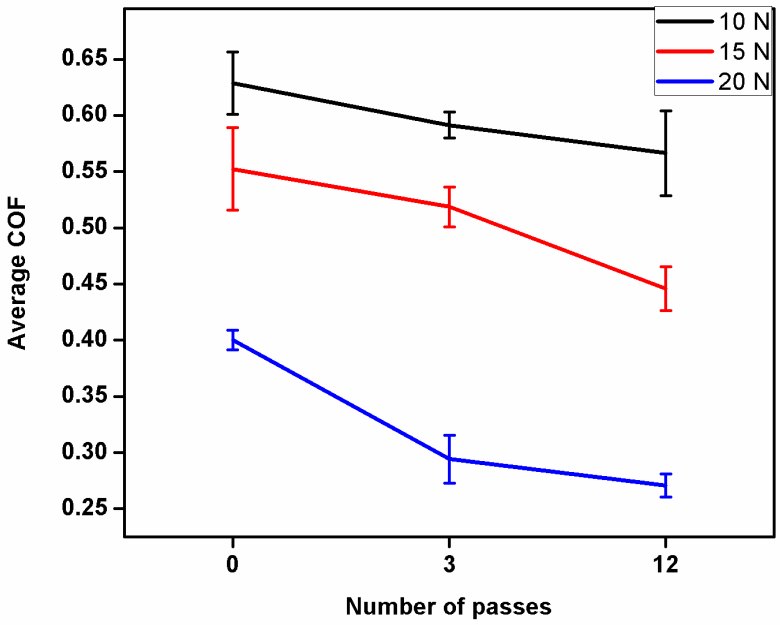

Fig.31. Average COF values for different MAF passes

A lower coefficient of friction and higher resistance to scratch are the desirable conditions for tribological applications. Fig.31 shows that there is a decrease in COF with an increase in number of MAF passes. As soon as the sliding starts the surface of the samples undergo deformation leading to scratching by wear particles, which is comparatively larger in coarse grained materials due to their low hardness. But the fine grained materials with higher hardness have the property to oppose deformation, thus allowing it to slide easily over the counterface with less energy expenditure. Also, according to Hall-Petch equation stated in equation (1), grain refinement leads to an increase in the strength of a material. So, the 12 pass MAFed sample has the lowest coefficient of friction which makes it suitable for tribocorrosion applications.

5.5.2.3. Effect of number of MAF passes on wear volume

Fig.32 shows the variation of wear volume for the as-received, 3 pass, and 12 pass samples of 316L SS at different loads of 10 N, 15 N, and 20 N. Wear volume is calculated by measuring the weight loss and density of the sample as per the equation (3). The different contributions for weight loss include:

- mechanical wear due to sliding of the pin samples against the counterface
- dissolution of metal surface due to the removal of passive film

$$\text{Wear volume} = \frac{\text{weight loss}}{\text{density}} \tag{3}$$

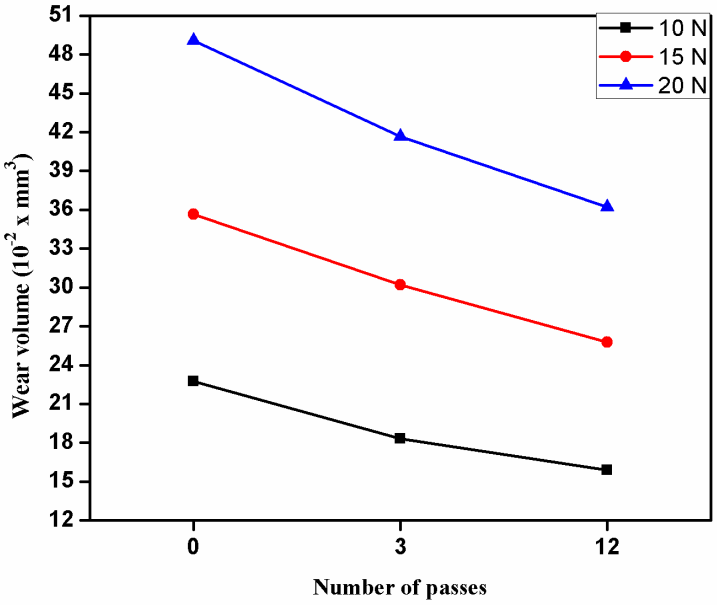

Fig.32. Variation of wear volume for MAFed samples of 316L SS at normal loads of 10 N, 15 N, and 20 N

From Fig.32, it is evident that with an increase in load for a particular condition of sample, there is always a substantial increase in the wear volume. This may be attributed to the high contact pressures acting on the surface of the sample at high loads and thus resulting in a comparatively high removal or wear of the material. This can also be explained from the Archard equation [33], stated in equation (4).

$$V = \frac{KWL}{H} \quad (4)$$

where V, K, W, L, and H represents the total wear volume, Archard wear coefficient, total normal load, sliding distance, and hardness of the softest contacting surfaces i.e., the sample surface respectively.

The equation (4) above implies that the total wear volume is directly proportional to the normal load applied. So, it can be concluded that the wear volume increases with an increase in normal load.

Fig.32 also shows that at a constant load, there is a gradual decrease in wear volume as the number of passes of MAF increased. This is attributed to the increase in hardness with the increase in number of MAF passes as shown in Fig.8. The 12 pass 316L SS sample which has the highest hardness, restricts the tendency of deformation and wear during sliding, thus proving to be the highest wear resistant material. This can be explained from the Archard equation (4), where the total wear volume is inversely proportional to the hardness of the sample. Therefore, it can be concluded that at a constant load, the wear volume decreases with an increase in the number of MAF passes.

5.5.2.4. Effect of number of MAF passes on wear rate

Fig.33 shows the variation of wear rate of as-received, 3 pass, and 12 pass MAFed 316L SS samples at different contact loads of 10 N, 15 N, and 20N. Wear rate is calculated [34] by using the equation (5). A detailed method to calculate wear rate is shown below.

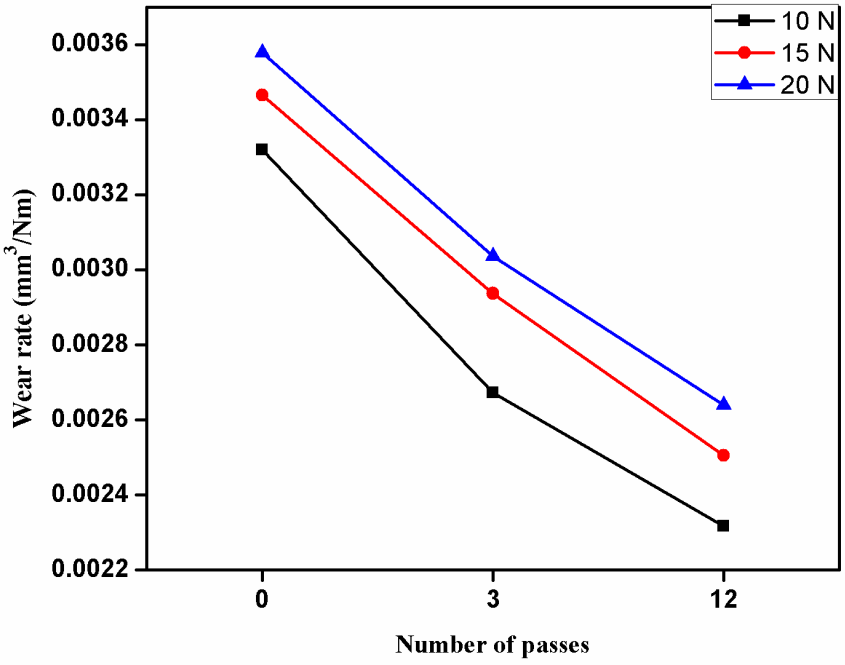

Fig.33. Variation of wear rate for MAFed samples of 316L SS at normal loads of 10 N, 15 N, and 20 N

Wear rate calculation:

Wear diameter = 0.04 m

rpm of disc = 60

Time = 5000 s

Speed = (∏ x rpm of disc x wear diameter) / 60

= 0.1257 m/s

Sliding distance = speed x time

= 628.5714 m

Volume (mm^3) = weight loss (g) / Density (g/mm^3)

$$\text{Wear rate} = \frac{\text{Wear Volume}}{\text{Load x sliding distance}},\ mm^3/Nm \qquad (5)$$

From Fig.33 it is observed that, for a particular sample, with an increase in load there is an increase in wear rate. This is in accordance to the increase in wear volume as shown in Fig. 32. Also at higher loads, the passive film breaks easily, which is eliminated as wear debris. The process of formation and deterioration of passive film continues during sliding, which results in increasingly severe wear.

At a constant load, the wear rate is decreasing with increase in number of MAF passes, which proves that grain refinement has a significant effect on wear resistance. This improvement in wear resistance helps to contribute in certain tribologocial applications.

5.5.2.5. Characterization of tribo-corroded surface

Fig.34 shows the SEM images of the worn surfaces of the as-received, 3 pass, and 12 pass specimens at different loads of 10 N, 15 N, and 20 N.

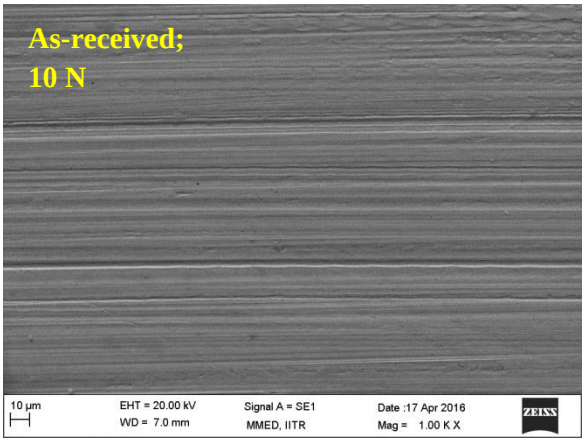

(a)

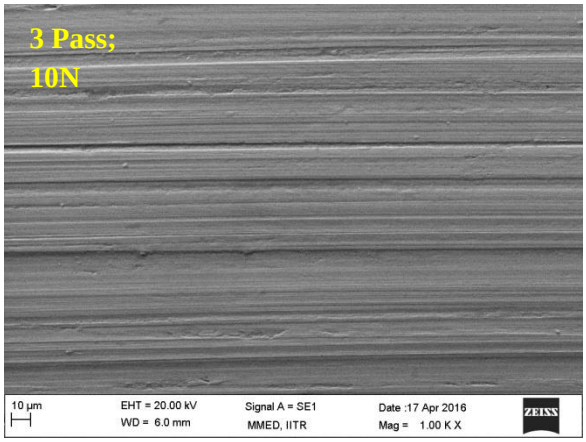

(b)

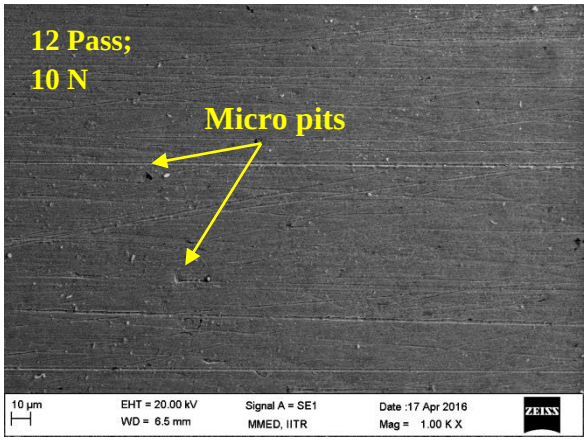

(c)

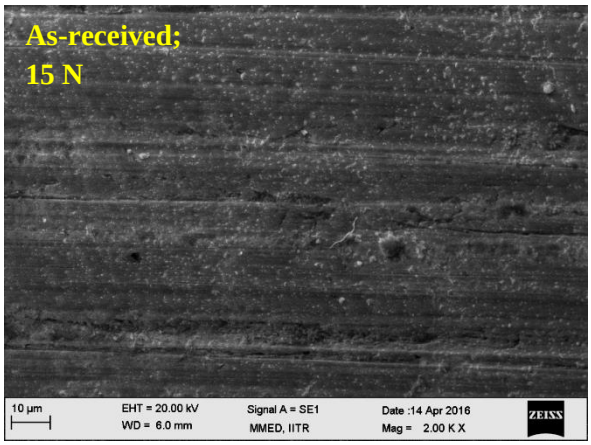
As-received;
15 N
10 µm
EHT = 20.00 kV
WD = 6.0 mm
Signal A = SE1
MMED, IITR
Date :14 Apr 2016
Mag = 2.00 K X
ZEISS

(d)

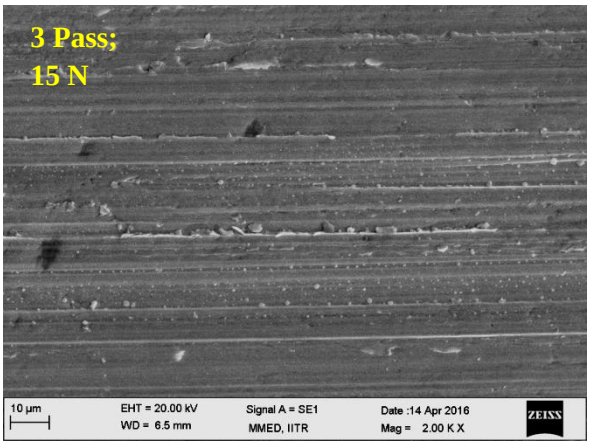
3 Pass;
15 N
10 µm
EHT = 20.00 kV
WD = 6.5 mm
Signal A = SE1
MMED, IITR
Date :14 Apr 2016
Mag = 2.00 K X
ZEISS

(e)

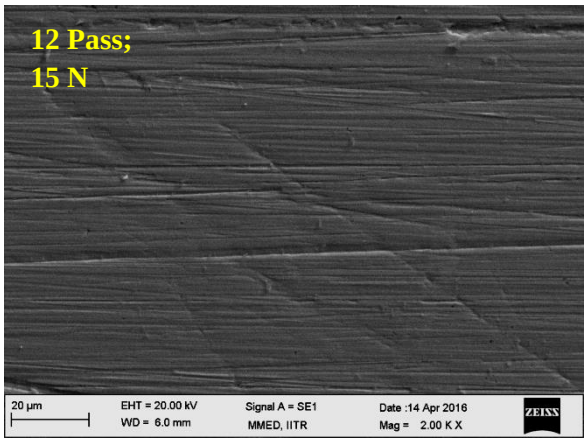
12 Pass;
15 N
20 µm
EHT = 20.00 kV
WD = 6.0 mm
Signal A = SE1
MMED, IITR
Date :14 Apr 2016
Mag = 2.00 K X
ZEISS

(f)

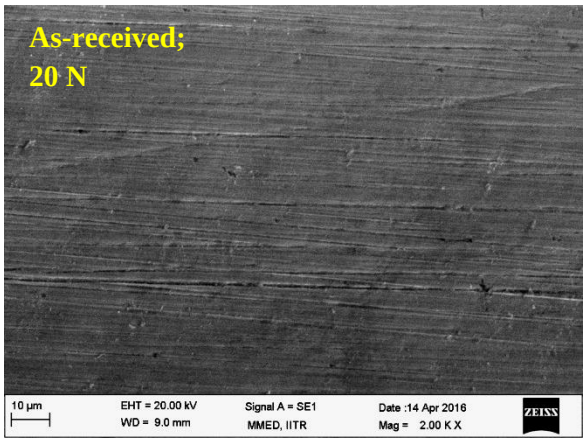
As-received;
20 N
10 µm
EHT = 20.00 kV
WD = 9.0 mm
Signal A = SE1
MMED, IITR
Date :14 Apr 2016
Mag = 2.00 K X
ZEISS

(g)

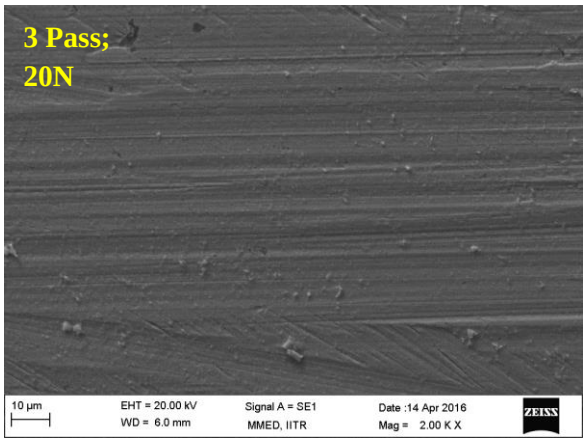
3 Pass;
20N
10 µm
EHT = 20.00 kV
WD = 6.0 mm
Signal A = SE1
MMED, IITR
Date :14 Apr 2016
Mag = 2.00 K X
ZEISS

(h)

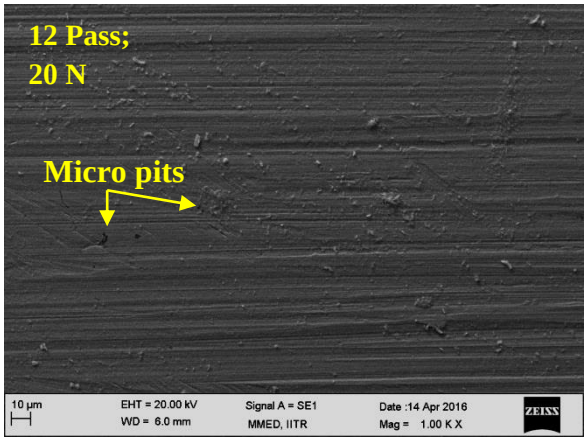

(i)

Fig.34. SEM micrographs of the tribo-corroded samples of as-received, 3 pass, and 12 pass under different contact loads of 10 N (a,b,c), 15 N (d,e,f) , and 20 N (g,h,i)

Irrespective of the test material, all the wear tracks in Fig.34 are characterized by large number of scratching marks. This is attributed to the abrasive wear mechanism which is not only due to the sliding against the hard alumina counterface, but also due to the third body or the worn particles between the sample and the counterface.

From the Fig.34, it is observed that, with an increase in normal load for a particular condition sample, the scratch depth has increased i.e., there is an increase in wear volume. The damage caused to the sample is therefore directly proportional to the applied normal load [35]. Also, the wear scratches started to become wider as the normal load increased. During sliding, the worn surface will be at an electrochemically active state. Hence, the wear debris ejected out due to the abrasion action gets oxidized. This corrosion product of wear debris produces deep abrasive scratches by the phenomenon of 3-body abrasion [36]. Also, at a constant load, the 12 pass sample has shallower scratches which are attributed to its relatively higher hardness.

During sliding, the passive film on the sample surface gets damaged. Hence, there were micro-pits formed on the surface. The pits affect the OCP value by shifting to more negative potentials as shown in Fig.28.

5.5.3. POTENTIODYNAMIC POLARIZATION BEHAVIOUR

Potentiodynamic polarization measurements help to understand the complete corrosion and tribocorrosion behaviour of the samples. Fig.35 (a), (b), and (c) shows the polarization curves of the as-received, 3 pass, and 12 pass MAFed samples respectively, in Hanks' solution. During non-sliding condition, as the sample is not in contact with the counterface, the polarization curves thus obtained help to understand the stability of passive films without the effect of mechanical damage.

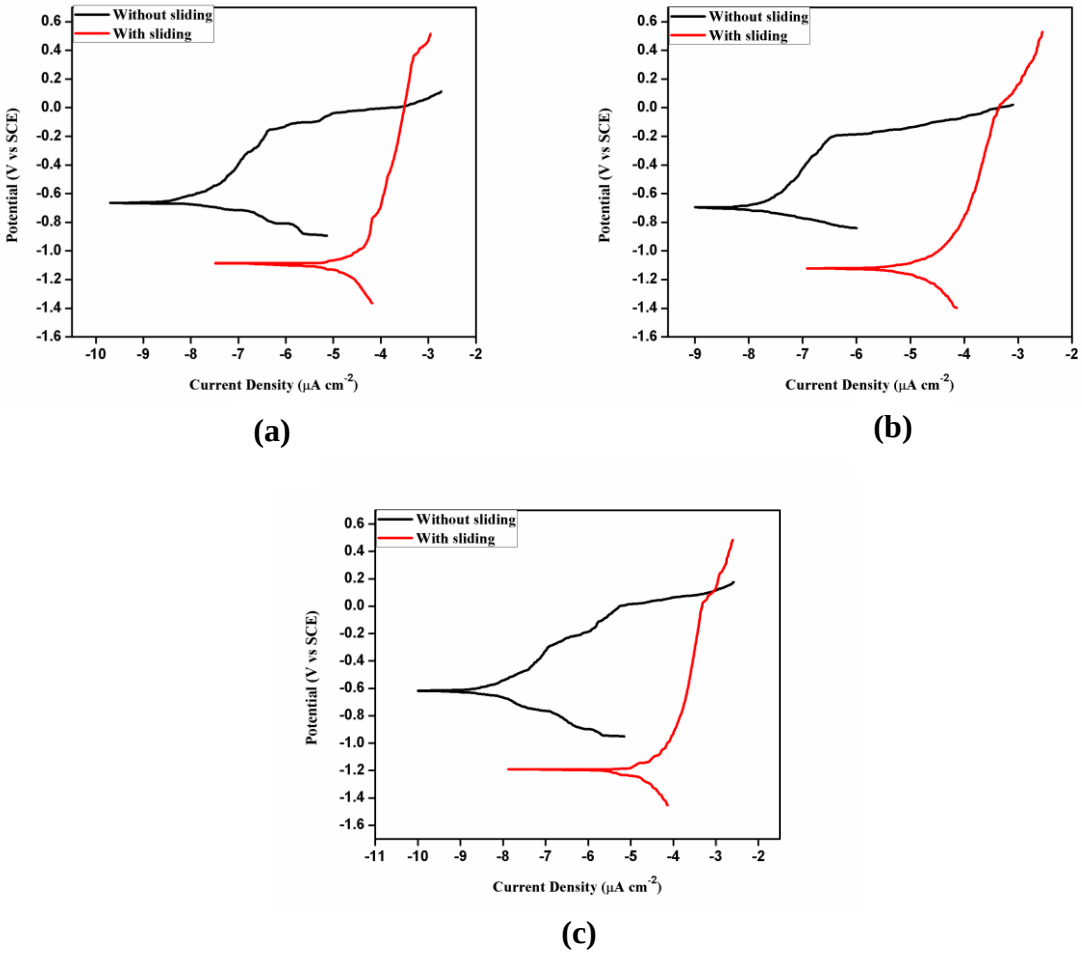

Fig.35. Potentiodynamic polarization curves of (a) as-received (b) 3 pass, and (c) 12 pass MAFed 316L SS samples showing a comparison between with sliding and non-sliding conditions

From Fig.35, it is clear that the all the three samples of 316L SS exhibit similar potentiodynamic polarization behaviour during without sliding condition. Above the corrosion potential i.e., at the anodic potentials there is a spontaneous passive film formation and its breakdown in the potential range of -0.2 V to 0.0 V. As the passive film breaks, there is a sudden increase in the current density indicating the initiation of pitting corrosion. As compared to the as-received and 3 pass samples, the 12 pass sample showed higher breakdown potential which can be attributed to its UFG structure and less dislocation density inside the grains.

The polarization curves during sliding help to know the repassivating ability of steel when the passive film gets damaged or removed due to the mechanical contact between the pin sample and the counterface. During sliding condition, the potentiodynamic behaviour of as-received, 3 pass and 12 pass samples is greatly different from its non-sliding polarization behaviour.

From Fig.33, firstly it is observed that there is a shift of the zero potential or the corrosion potential to lower and more active potentials by more than 0.3 V compared to curves of without sliding condition. This lowering of potential is due to the mechanical damage caused to the passive film during sliding which results in the activation of worn surface. Secondly, there is an increase in anodic current density by about four orders of magnitude compared to the curves of non-sliding specimen. This significant increase in current density can be attributed to the activation of worn surface when the passive film gets damaged and thus favouring the formation of micro pits in the Hanks' solution. So the two factors responsible for wear-induced corrosion can be concluded as anodic dissolution and pit formation. There is a decrease in breakdown potential for the 3 pass and 12 pass samples during sliding which is due to the low adherence and easy breakdown of passive film during sliding.

The as-received and MAFed samples showed almost a similar anodic polarization behaviour in tribocorrosion, but with a slight increase in breakdown potential during non-sliding for the MAFed samples. Therefore, it can be said that MAF has slightly improved the pitting resistance during non-sliding evaluation of 316L SS. This can be attributed to the UFG structure with less dislocation density. But, there is a decrease in breakdown potential to active values during sliding experiments, thus proving that MAF has affected the polarization behaviour during sliding.

CHAPTER 6: CONCLUSIONS

The present study explores the possibility of strengthening of 316L stainless steel through grain refinement using warm multi-axial forging. Microstructural, mechanical, corrosion and tribocorrosion behaviour of the UFG 316L SS is evaluated to assess its suitability in medical implants and other industrial applications.

(a) By warm MAF, considerable grain refinement was achieved in 316L SS. The material also retained its austenitic structure even after 12 passes of MAF. As the number of MAF passes increased, the material attained a UFG structure by cDRX. The average grain size of as-received sample decreased from 155 μm to 151.2 nm for the MAFed 12 pass sample.

(b) Hardness of the as-received 316L SS increased rapidly from 223 VHN to 290 VHN for the sample MAFed to 3 passes, after which there was a marginal increase only for the subsequent passes. This can be attributed to the combined effect of Hall-Petch strengthening and strain hardening.

(c) The potentiodynamic Tafel results showed that there was only a slight increase in uniform corrosion rate of 316L SS in Hanks' solution and 3.5 wt% NaCl solution even after 12 MAF passes. This can be attributed to the competitive effect of increment of grain boundary volume pertaining from grain refinement and low dislocation density in the UFG structure.

(d) The cyclic polarisation test has showed an increase in passive range and decrease in area of the cyclic loop for the 12 pass MAFed sample in Hanks' solution, thus proving to be a better pitting corrosion resistant material when compared to the as-received sample. This can be attributed to an increase in grain boundary volume and homogenization of pit-inducing impurities and non-metallic phases due to SPD. Also, cyclic polarisation behaviour is unaffected in 3.5wt% NaCl solution even after MAF.

(e) Tribocorrosion behaviour was evaluated by performing sliding tests at OCP. For the 12 pass sample, there is a comparative rise of the OCP value which is due to the UFG structure with less dislocation density in the grains. With an increase in number of MAF passes, there is a decrease in COF, wear volume, and wear rate which may be attributed to the increase in hardness and UFG structure. This improvement in wear resistance helps to contribute in certain tribologocial applications.

(f) Potentiodynamic polarization behaviour showed a significant decrease in OCP value and increase in current density during sliding when compared to the non-sliding condition. This is due to the easy removal of passive film during sliding, leading to anodic dissolution and pit formation. UFG material has attained an increase in breakdown potential during non-sliding condition, thus proving to have a comparatively pitting corrosion resistance.

(g) There is an improvement in localized corrosion behaviour and sliding wear resistance of UFG 316L SS. Thus, it has potential for use in tribological applications.

FUTURE SCOPE

(1) There is a noticeable grain refinement which leads to an improvement in yield strength. So, tensile testing can be done to find out the improvement in the strength of the material.

(2) The effect of deformation on the defect density can be evaluated by Mott-Schottky analysis. The defect density is believed to be higher because of the deformation that was induced. This can be studied and compared.

CHAPTER 7: REFERENCES

[1] M Eskandari, AZ Hanzaki, HR Abedi, An investigation into the room temperature mechanical properties of nanocrystalline austenitic stainless steels, Mat. & Des., 45 (2013) 674–681.

[2] XH Chen, J Lu, L Lu, K Lu, Tensile properties of a nanocrystalline 316L austenitic stainless steel, Scrip. Mater., 52 (2005) 1039-1044.

[3] TG Nieh, LM Hsiung, J Wadsworth, R Kaibyshev, Hall-Petch relation in nanocrystalline solids, Acta Mater., 46 (1998) 2789-2795.

[4] RZ Valiev, Bulk nanostructured materials from severe plastic deformation, Prog. Mat. Sci., 45 (2000) 103-89.

[5] AK Padap, GP Chaudhari , V Pancholi, SK Nath, Warm multiaxial forging of AISI 1016 steel, Mat. & Des., 31 (2010) 3816–3824.

[6] Y Sun, V Rana, Tribocorrosion behaviour of AISI 304 stainless steel in 0.5 M NaCl solution, Mat. Chem. & Phy., 129 (2011) 138– 147.

[7] A Mogucheva, N Lopatin, A Belyakov, R Kaibyshev, Grain refinement in austenitic stainless steel during warm screw rolling, Mat. Sci. Forum, 715-716 (2012) 889-894.

[8] Z.J Zheng, Y Gao, A hybrid refining mechanism of microstructure of 304 stainless steel subjected to ECAP at 500 °C, Mat. Sci. Eng. A, 639 (2015) 615–625.

[9] W Pachla, J Skiba, Nanostructurization of 316L type austenitic stainless steels by hydrostatic extrusion, Mat. Sci. Eng. A, 615 (2014) 116–127.

[10] B Roy, R Kumar, Effect of cryorolling on the microstructure and tensile properties of bulk nano-austenitic stainless steel, Mat. Sci. Eng. A, 631 (2015) 241-247.

[11] M Eskandari, A Najafizadeh, A Kermanpur, Effect of strain-induced martensite on the formation of nanocrystalline 316L stainless steel after cold rolling and annealing, Mat. Sci. Eng. A, 519 (2009) 46-50.

[12] H Wang, I Shuro, Annealing behavior of nano-crystalline austenitic SUS316L produced by HPT, Mat. Sci. Eng. A, 556 (2012) 906-910.

[13] Y Idell, G Facco, Strenghtening of austenitic stainless steel by formation of nanocrystalline γ-phase through severe plastic deformation during two-dimensional linear plane-strain machining, Scripta Mater., 68 (2013) 667–670.

[14] A Breu, FG Hamilton, Deformation induced martensite in an AISI 301LN stainless steel: characterization and influence on pitting corrosion resistance, Mat. Res., 10 (2007) 1980-5373.

[15] Y Nakao, H Miura, Nano-grain evolution in austenitic stainless steel during multidirectional forging, Mater. Sci. Eng. A, 528 (2011) 1310-1317.

[16] BJ Han, Z Xu, Grain refinement mechanism of Fe-32 Ni alloys during multiaxial forging, Mat. Sci. Tech., 22 (2006) 1359-63.

[17] A Belyakov, K Tsuzaki, Y Kimura, Regularities of deformation microstructures in ferritic stainless steels during large strain cold working, ISIJ International, 48 (2008) 1071-1079.

[18] A Belyakov, K Tsuzaki, R Kaibyshev, Nanostructure evolution in an austenitic stainless steel subjected to Multiple Forging at Ambient Temperature, Mat. Sci. Forum, 667-669 (2011) 553-558.

[19] J Huang, Z Xu, Evolution mechanism of grain refinement based on dynamic recrystallisation in multiaxially forged austenite, Mater. Lett., 60 (2006) 1854-1858.

[20] M Tikhonova, A Belyakov, R Kaibyshev, Kinetics of grain refinement by warm deformation of 304 type stainless steel, Mater. Sci. Forum, 706-709 (2012) 2326-2331.

[21] O Sitidikov, T Sakai, A Goloborodko, H Miura, Effect of pass strain on grain refinement in 7475 alloy during hot multidirectional forging, Philos. Mag. A, 85 (2005) 1159-1175.

[22] Q Guo, HG Yan, ZH Chen, Grain refinement in as-cast AZ80 Mg alloy under large strain deformation, Mater. Charact., 58 (2007) 162-167.

[23] N Diomidis, JPCelis, P Ponthiaux, F Wenger, Tribocorrosion of stainless steel in sulphuric acid: identification of corrosion–wear contributions and effect of contact area, Wear, 269 (2010) 93–103.

[24] Y Sun, E Haruman, Tribocorrosion behaviour of low temperature plasma carburized 316L stainless steel in 0.5M NaCl solution, Corr. Sci., 53 (2011) 4131–4140.

[25] KS Suresh, M Geetha, Effect of equal channel angular extrusion on wear and corrosion behaviour of the orthopaedic Ti–13Nb–13Zr alloy in simulated body fluid, Mat. Sci. Eng. C, 32 (2012) 763–771.

[26] D Holmes, S Sharifi, Tribo-corrosion of steel in artificial saliva, Tribology International, 75 (2014) 80–86.

[27] M Salasi, G Stachowiak, Tribo-electrochemical behaviour of 316L stainless steel: The effects of contact configuration, tangential speed, and wear mechanism, Corr. Sci., 98 (2015) 20–32.

[28] BQ Han, Z Lee, D Witkin, S Nutt, EJ Lavernia, Deformation behaviour of bimodal nanostructured 5083 Al alloys, Metall. Mater. Trans. A, 36 (2005) 957–65.

[29] M Stern, RM Roth, Standard test method for conducting potentiodynamic polarization resistance measurements, Journal of electrochemical society, 104 (1957) 390.

[30] SV Muley, AN Vidvans, GP Chaudhari, An assessment of ultra fine grained 316L stainless steel for implant applications, Acta Bio., 30 (2016) 408-419.

[31] J Chen, Q Zhang, Q Li, Corrosion and tribocorrosion behaviours of AISI 316 stainless steel and Ti6AlV alloys in artificial sea water, Trans. Nonferrous Met. Soc. China, 24 (2014) 1022-1031.

[32] F Ahmad, SH Jason, M Aslam, A Haziq, Tribology behaviour of aluminium particles reinforced aluminium matrix composites and brake disc materials, Procedia Engg., 68 (2013) 674-680.

[33] JF Archard, Contact and rubbing of flat surfaces, Appl. Phys., 24 (1953) 981-988.

[34] V Lakshminarayana, VP Balu, Influence of varying load on wear rate and frictional resistance of EN-8 steel sliding against EN-31 steel, ARPN journal of Engg. & applied Sci., 10 (2015) 1819-6608.

[35] E Mardare, L Benea, JP Celis, Importance of applied normal loads on the tribocorrosion behaviour of Ti-6Al-4V alloy in bio-simulated environment, Surface and interfaced Engg. Mat., 42 (2012) 474-78.

[33] FB Saada, Z Antar, K Elleuch, P Ponthiaux, On the tribocorrosion behaviour of 304L stainless steel in olive pomace / tapwater filtrate, Wear, 328-329 (2015) 509-517.